


## Accuracy of metaGGA functionals in describing transition metal fluorides

Dereje Bekele Tekliye  and Gopalakrishnan Sai Gautam <sup>\*</sup>*Department of Materials Engineering, Indian Institute of Science, Bengaluru, 560012, Karnataka, India* (Received 19 January 2024; revised 2 July 2024; accepted 28 August 2024; published 12 September 2024)

Accurate predictions of material properties within the chemical space of transition metal fluorides (TMFs), using computational frameworks such as density functional theory (DFT), is important for advancing several technological applications. The state-of-the-art semilocal exchange-correlation functionals within DFT include the strongly constrained and appropriately normed (SCAN) and the restored regularized SCAN ( $r^2$ SCAN), both of which are meta generalized gradient approximation (metaGGA) functionals. Given their semilocal nature, both SCAN and  $r^2$ SCAN are susceptible to self-interaction errors (SIEs) while modeling highly correlated  $d$  electrons of transition metals. Hence, in this work, we evaluate the accuracy of both SCAN and  $r^2$ SCAN functionals in estimating several properties of TMFs, including redox enthalpies, lattice geometries, on-site magnetic moments, and band gaps. Specifically, we consider binary fluorides of Ti, V, Cr, Mn, Fe, Co, Ni, and Cu. We observe both SCAN and  $r^2$ SCAN exhibit poor accuracy in estimating fluorination enthalpies among TMFs, which can be primarily attributed to SIEs among the  $d$  electrons, given both functionals bind  $F_2$  accurately. Thus, we derive optimal Hubbard  $U$  corrections for both functionals based on experimental fluorination (or oxidation) enthalpies within binary TMFs. Note that our attempts at using the linear response theory to derive  $U$  corrections yielded unphysical values for V, Fe, and Ni fluorides. While adding the fluorination-enthalpy-derived  $U$  corrections to the metaGGA functionals does not significantly affect the lattice volumes and on-site magnetic moments (and in turn, the accuracy of these property estimations versus experiments), it does cause a significant increase in calculated band gaps. Note that the  $U$ -corrected band gaps in several fluorides deviate to a lesser extent from band gaps calculated with a hybrid functional compared to the non- $U$ -corrected functionals. Also, we calculated the average Na intercalation voltage in Mn, Fe, Co, and Ni fluorides, and stabilities of Na-V-F, Na-Cr-F, Na-Mn-F, and Na-Fe-F ternary compounds as transferability checks of our optimal  $U$  values. Overall, we do recommend the incorporation of the Hubbard  $U$  correction to improve predictions of redox enthalpies in other TMFs. Finally, our study should advance the accuracy of DFT-based screening studies to unearth novel TMFs, which can be used in various applications, including energy storage, catalysis, and magnetic devices.

DOI: [10.1103/PhysRevMaterials.8.093801](https://doi.org/10.1103/PhysRevMaterials.8.093801)

## I. INTRODUCTION

Redox-active  $3d$  transition metal fluorides (TMFs) are widely studied and have been used in the fields of magnetism [1,2], catalysis [3–6], electroceramics [7–9], and electrochemical energy storage [10–18]. For instance, fluorides exhibit considerable promise as prospective positive electrode (cathode) materials for batteries owing to the advantageous inductive effect associated with fluorine [19]. Characterized by fluorine's high electronegativity, fluorine addition to a cathode material typically yields higher voltages and higher energy densities. Several fluoride-based cathode materials, such as  $\text{LiMnF}_3$ ,  $\text{NaFeF}_3$ ,  $\text{NaMnF}_3$ ,  $\text{NaCoF}_3$ , and  $\text{KVO}_4\text{F}$ , have been investigated as potential candidates for intercalation-type and conversion-type rechargeable lithium-ion, sodium-ion, and potassium-ion batteries [20–24]. Other notable conversion-based electrodes in the lithium-ion chemical space include the  $\text{LiF} + \text{FeF}_2 - \text{LiFeF}_3$  and  $\text{LiF-FeO}$  systems, which are fluoride-based as well [16,25–28].

Investigating materials for energy storage and other applications, including identifying new materials and understanding the underlying properties of existing materials, has greatly benefited from the utilization of quantum mechanical methods [29–34], such as density functional theory (DFT [35,36]). Notably, the choice of the exchange-correlation (XC) functional in DFT plays a crucial role in accurately describing the electronic interactions within a given material, and hence its resultant properties, such as redox enthalpies and ground state atomic configurations. Prominent XC functionals include the local density approximation (LDA [36]), the generalized gradient approximation (GGA [37]), and the meta-generalized gradient approximation (metaGGA [38–40]), which represent increasing levels of accuracy, as illustrated using the Jacob's ladder analogy [41].

Among metaGGA functionals, the strongly constrained and appropriately normed (SCAN [38]) functional satisfies all the 17 known constraints of an XC functional. SCAN incorporates the orbital kinetic energy density as a parameter in addition to the local electron density and its gradient, resulting in higher accuracy [42–45]. However, SCAN suffers from numerical instability and associated computational convergence difficulties [39]. To address SCAN's shortcomings,

<sup>\*</sup>Contact author: saigautam@iisc.ac.in

the restored regularized SCAN ( $r^2$ SCAN [40]) functional has been developed.  $r^2$ SCAN combines the numerical accuracy of SCAN with improved numerical stability [46–48], while satisfying 16 out of the 17 known constraints for an XC functional. Thus, SCAN and  $r^2$ SCAN represent the state-of-the-art metaGGA functionals and have been widely used for both materials discovery and improving fundamental understanding [49–55].

Employing metaGGA functionals to predict and investigate correlated electron systems, such as TMFs, can still provide an erroneous description of the underlying electronic structure. For example, both SCAN and  $r^2$ SCAN exhibit residual self-interaction errors (SIEs [56]) while modeling transition metal oxides (TMOs), which are also highly correlated systems like TMFs. The residual SIEs often result in incorrect redox enthalpies, ground state polymorphs, lattice parameters, on-site magnetic moments, and electronic properties [47,57–59]. Typically, functionals suffer from SIEs owing to an overestimation of electronic delocalization within contracted and localized  $d$  and/or  $f$  orbitals. Thus any residual SIE is likely to influence the accuracy of the metaGGA functionals in modeling TMFs as well. One potential way of mitigating SIEs in correlated systems is adding a Hubbard  $U$  correction [60] (on the  $d$  and/or  $f$  orbitals) to the semilocal functionals. Adding the  $U$  correction has been shown to remove several of the spurious predictions by SCAN and  $r^2$ SCAN in the TMO chemical space [47,57,58]. Thus, it is useful to explore the accuracy of such Hubbard  $U$ -corrected metaGGA frameworks, specifically SCAN+ $U$  and  $r^2$ SCAN+ $U$ , on property predictions within TMFs. However, the magnitude of the  $U$  correction is not known *a priori*.

Several techniques, with their own sets of pros and cons, have been used to identify an "optimal"  $U$  correction for a given transition metal (TM) system, including (1) theory-based approaches, such as linear response theory [61–65], embedded Hartree-Fock calculations [66,67], constrained random phase approximation (cRPA) [68], and pseudohybrid Agapito-Curtarolo-Buongiorno-Nardelli (ACBN0) [69] functional, (2) statistics-based approaches, such as machine learning-based Bayesian optimization [70], and clustering-validation techniques [71], and (3) using experimental data, such as oxidation enthalpies [57,58,72–74] and band gaps [75]. Statistics-based and experimental-data-based approaches typically provide an averaged  $U$  correction for a given TM, i.e., a  $U$  value that can be used across multiple oxidation states of the TM, while theoretical approaches provide an oxidation-state-specific (and often structure-specific)  $U$  correction.

Notably, previous studies have utilized experimental oxidation enthalpies to estimate optimal  $U$  corrections for different functionals (e.g., GGA [72], SCAN [57,58], and  $r^2$ SCAN [47]) and for several TMs in oxide coordination. In turn, such  $U$  corrections have been used successfully in several materials screening [32,76] and optimization [77–79] studies. However, such a widespread identification of optimal  $U$  corrections that can be used with SCAN or  $r^2$ SCAN in the TMF chemical space has not been done, so far.

In this work, we present a comprehensive investigation assessing the accuracy of the SCAN and the  $r^2$ SCAN metaGGA

functionals, and their Hubbard  $U$  corrected frameworks, in predicting the redox thermodynamics, lattice parameters, magnetic properties, and electronic structures of several TMFs. We verify that both SCAN and  $r^2$ SCAN estimate the binding energy of  $F_2$  accurately. We identify an optimal  $U$  correction, if necessary, by considering experimental oxidation (i.e., fluorination) enthalpies of binary  $3d$  TMFs, where the TMs are Ti, V, Cr, Mn, Fe, Co, Ni, or Cu. For a few compounds, we also use the linear response theory to demonstrate that the framework does provide unphysical  $U$  corrections compared to the experimental-data-derived values. Overall, both SCAN and  $r^2$ SCAN exhibit similar errors in calculating properties across several TMFs, with their  $U$ -corrected versions exhibiting similar improvements in accuracies compared to the corresponding "bare" functionals. Wherever possible, we verified the transferability of our  $U$  values by calculating properties of compounds not used in estimating the  $U$  values. Our work should provide a set of guidelines for computational screening approaches to more accurately predict properties within the correlated TMF space for energy storage and other applications.

## II. METHODS

### A. Computational methods

All spin-polarized SCAN(+ $U$ ), and  $r^2$ SCAN(+ $U$ ) calculations were performed using the Vienna *ab initio* simulation package (VASP [80,81]), using the frozen-core projector augmented wave (PAW [82,83]) potentials, as listed in Table S1 of the Supplemental Material (SM) [84]. We used the rotationally invariant Hubbard  $U$  approach developed by Dudarev *et al.* [85] in our calculations. The electronic kinetic energy was expanded using plane waves up to an energy of 520 eV. We employed a Gaussian smearing of width 0.05 eV to integrate the Fermi surface. We sampled the irreducible Brillouin zone with  $\Gamma$ -centered Monkhorst-Pack [86]  $k$ -point grids of a minimum density of 48  $k$  points per  $\text{\AA}$  (i.e., a real space lattice vector of 1  $\text{\AA}$  was sampled using 48 subdivisions in the reciprocal space). The total energy and atomic force convergence criteria were set to  $10^{-5}$  eV and  $|0.03|$  eV/ $\text{\AA}$ , respectively, with no symmetry being preserved during relaxations of the cell volume, cell shape, and ionic positions within each structure. To calculate the binding energy of  $F_2$  gas, we performed two calculations, one with an isolated  $F_2$  molecule and another with an isolated F atom in  $18 \text{\AA} \times 19 \text{\AA} \times 20 \text{\AA}$  asymmetric cells, and allowed the atomic positions to change in  $F_2$ .

The initial structures of all compounds were obtained from the inorganic crystal structure database (ICSD [87]). We utilized the conventional cell for all systems, except CuF and  $MnF_3$ . In CuF we used a  $2 \times 2 \times 2$  supercell due to convergence difficulties associated with our electronic density of states (DOS) calculations with the conventional cell. In the case of  $MnF_3$ , we used a  $2 \times 2 \times 2$  supercell to account for the A-type ( $\uparrow\uparrow\downarrow\downarrow$ ) antiferromagnetic (AFM) ordering [88]. Unless specified, we initialised the on-site magnetic moment of a TM to its corresponding high spin configuration.

For band gap calculation of TMFs, we used the generalized Kohn-Sham technique [89] and calculated the DOS for all systems considered. We used the optimized structure and the

initial charge density from a prior structure relaxation for all DOS calculations. Subsequently, we introduced a set of zero-weighted  $k$  points, corresponding to a density of 96  $k$  points per Å, with the  $k$  points that were used for the structure relaxation retained their original weights. Finally, we performed a single self-consistent-field (SCF) calculation for each structure, sampling the electronic DOS over an energy range of  $-20$  to  $20$  eV at intervals of  $0.005$  eV. The total energy convergence criterion was set to  $10^{-6}$  eV in all DOS calculations. For select TMFs, we also performed DOS calculations using the Heyd-Scuseria-Ernzerhof (HSE06 [90,91]) hybrid functional for comparison with SCAN(+ $U$ ) and  $r^2$ SCAN(+ $U$ ) calculations. For HSE06-DOS calculations, we used the relaxed SCAN+ $U$  structures and sampled the irreducible Brillouin zone with a density of 16  $k$  points per Å.

### B. Reaction energies and optimal $U$

We used experimental oxidation (i.e., fluorination) enthalpy per  $F_2$  ( $\Delta H_O^{\text{expt}}$ ) among binary TMFs to identify the optimal Hubbard  $U$  correction for each TM. Specifically, we considered reactions of the type  $MF_x + \frac{(y-x)}{2}F_2 \rightleftharpoons MF_y$ , where  $M = \text{Ti, V, Cr, Mn, Fe, Co, Ni, or Cu}$ . We collected the experimental thermochemical data (at 298 K, 1 atm) from the tables of the National Institute of Standards and Technology (NIST)-JANAF [92], Kubaschewski [93], Barin [94], and Wagman [95]. The experimental enthalpy of formation ( $\Delta H_f^{\text{expt}}$  at 298 K) of each compound considered is compiled in Table I. For  $\text{FeF}_3$ , and  $\text{NiF}_3$ , we obtained  $\Delta H_f^{\text{expt}}$  from other literature sources [96,97]. Note that we determined the thermochemical data obtained through bomb calorimetry to be more reliable for  $\text{FeF}_3$  compared to the values reported in the NIST-JANAF tables, as detailed in Sec. III. In the absence of an extrapolated value (from experimental data) of  $\Delta H_f^{\text{expt}}$  at 0 K, we considered the measured value of  $\Delta H_f^{\text{expt}}$  at 298 K to be equivalent to 0 K [98]. Wherever possible, we compared the accuracy of property predictions with optimal  $U$  values derived using both 298 K and 0 K experimental data.

We approximated the theoretical oxidation enthalpy ( $\Delta H_O^{\text{theo}}$ ), based on calculated 0 K DFT total energies (i.e.,  $H \approx E$ , thus ignoring  $p-V$  contributions), as  $\Delta H_O^{\text{theo}} = E_{\text{MF}_y}^{\text{DFT}+U} - E_{\text{MF}_x}^{\text{DFT}+U} - \frac{(y-x)}{2}E_{F_2}^{\text{DFT}}$ , where DFT indicates either SCAN or  $r^2$ SCAN.  $U = 0$  simply indicates a SCAN or  $r^2$ SCAN calculation without any Hubbard  $U$  correction. To find the appropriate  $U$  for a given fluorination reaction, we varied the  $U$  value till the  $\Delta H_O^{\text{theo}}$  matched the  $\Delta H_O^{\text{expt}}$ . In case of TMs with multiple oxidation states and multiple fluorination reactions, such as Mn and Cr, we determined the optimal  $U$  by averaging the appropriate  $U$  values obtained for the individual fluorination reactions (see Fig. S2 of the SM).

For TMFs involving V, Fe, and Ni, we employed the linear response theory [99] to estimate  $U$  corrections as well, to provide a point of comparison to the experimental-data-based  $U$  values. In linear response theory, the effective interaction parameter,  $U$ , associated with a specific site,  $I$ , in a structure is given as

$$U = (\chi_0^{-1} - \chi^{-1})_{II}, \quad (1)$$

TABLE I. Experimental enthalpy of formation ( $\Delta H_f^{\text{expt}}$  at 298 K), space group, ICSD collection code, and experimental on-site magnetic moments of TMFs. The  $\pm$  sign in the magnetic moment column indicates an antiferromagnetic configuration. In the absence of quantitative experimental magnetic moments, only the configuration-type such as AFM, NM, and FM is given. No experimental information on the magnetic configuration is available for  $\text{CrF}_4$ .

Compound	$\Delta H_f^{\text{expt}}$ (eV/atom)	Space group	ICSD collection code	On-site magnetic moment ( $\mu_B$ )
$\text{TiF}_3$	-3.713	$R\bar{3}cR$	16 649	AFM [100]
$\text{TiF}_4$	-3.414	$Pnma$	78 737	NM
$\text{VF}_3$	-3.272	$R\bar{3}cR$	30 624	$\pm 2.00$ [88]
$\text{VF}_4$	-2.904	$P121/n1$	65 785	$\pm 1.00$ [101]
$\text{CrF}_2$	-2.687	$P121/n1$	31 827	$\pm 3.60$ [102]
$\text{CrF}_3$	-2.997	$R\bar{3}cR$	25 828	$\pm 3.00$ [88]
$\text{CrF}_4$	-2.581	$P42/mnm$	78 778	-
$\text{MnF}_2$	2.954	$P42/mnm$	14 142	$\pm 5.00$ [103]
$\text{MnF}_3$	-2.770	$C12/c1$	19 080	$\pm 4.00$ [88]
$\text{MnF}_4$	-2.239	$I41/a$	62 068	$\pm 3.85$ [104]
$\text{FeF}_2$	-2.479	$P42/mnm$	9166	$\pm 3.75$ [105]
$\text{FeF}_3$	-2.628 [96]	$R\bar{3}cR$	41 120	$\pm 5.00$ [88]
$\text{CoF}_2$	-2.323	$P42/mnm$	9167	$\pm 2.57$ [106]
$\text{CoF}_3$	-2.043	$R\bar{3}cR$	16 672	$\pm 3.21$ [107]
$\text{NiF}_2$	-2.268	$P42/mnm$	9168	$\pm 1.99$ [108]
$\text{NiF}_3$	-2.114 [97]	$R\bar{3}R$	87 944	FM [109]
$\text{CuF}$	-0.346	$F\bar{4}3m$	52 273	NM
$\text{CuF}_2$	-1.834	$P121/n1$	71 833	$\pm 0.73$ [110]

where  $\chi$  and  $\chi_0$  are the interacting (or SCF) and noninteracting (or non-self-consistent-field [NSCF]) response functions, respectively, to an on-site applied perturbation potential ( $\alpha_I$ ) [99]. For our linear response calculations, we used a  $2 \times 2 \times 2$  supercell for V fluorides, and the corresponding conventional cells for Fe and Ni fluorides. We varied  $\alpha_I$  across  $-0.2$  eV,  $-0.1$  eV,  $+0.1$  eV, and  $+0.2$  eV for calculating the response functions.

### C. Crystal structures and magnetic configurations

Figure 1 displays the initial crystal structures of all 3d TMFs that we examined in this study, as obtained from the ICSD. The space groups and ICSD collection codes of all structures are compiled in Table I. Blue spheres/polyhedra in Fig. 1 indicate the TM/ $\text{MF}_6$  octahedra, and orange spheres indicate F atoms. The antiferromagnetic (AFM) and ferromagnetic (FM) configurations of TMFs that were considered in this work are compiled in Figs. S2 and S3 of the SM [84]. We did not consider any specific magnetic ordering for  $\text{CuF}$  and  $\text{TiF}_4$  owing to their nonmagnetic (NM)  $d^{10}$  and  $d^0$  electronic configurations, respectively.

$\text{CuF}$  is known to crystallize in a cubic symmetry with the  $F\bar{4}3m$  space group, and we show the  $2 \times 2 \times 2$  supercell of the primitive that we used in our calculations in Fig. 1 [111]. The  $\text{MF}_2$  ( $M = \text{Mn, Fe, Co, or Ni}$ ) compositions crystallize in the well-known tetragonal rutile-type structure in the  $P42/mnm$  space group [112,113], while  $\text{CrF}_2$  and  $\text{CuF}_2$  both

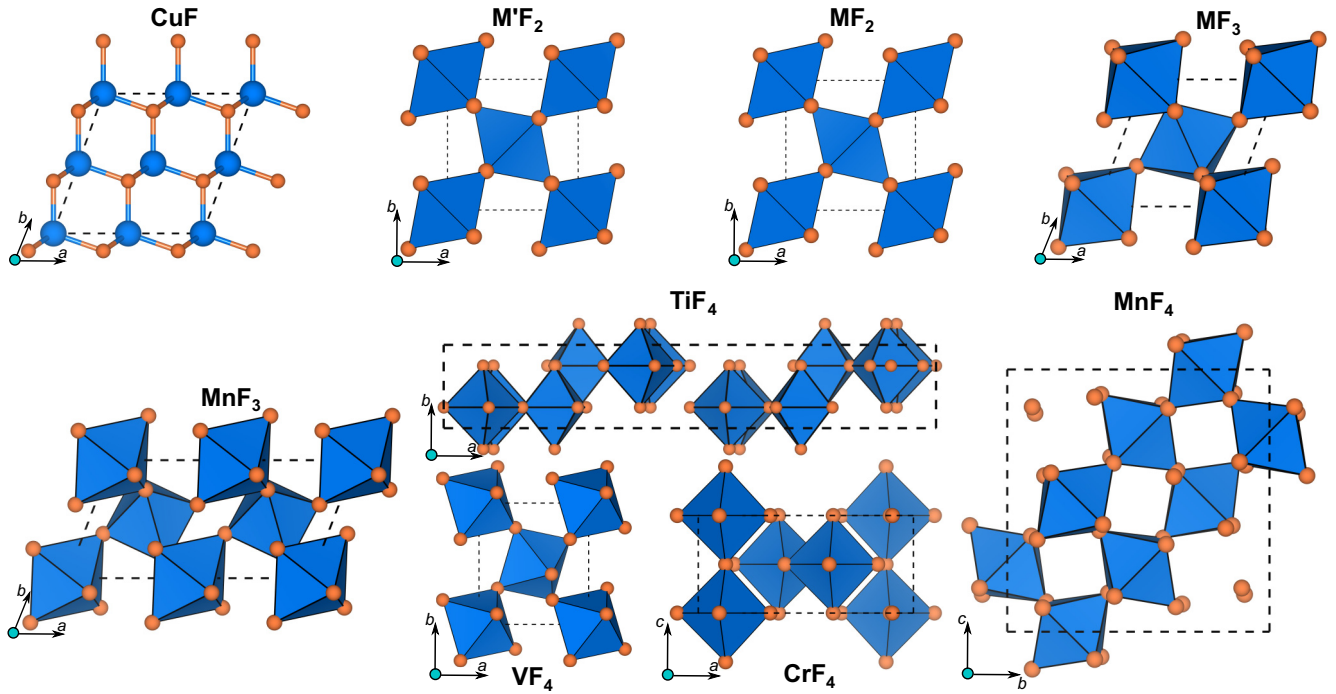


FIG. 1. The initial crystal structures of 3d TMFs.  $M'$  in  $M'F_2$  stands for Cr and Cu, and  $M$  in  $MF_2$  signifies Mn, Fe, Co, or Ni.  $M$  in  $MF_3$  indicates Ti, V, Cr, Fe, Co, or Ni. The 3d TM and F atoms are represented by blue spheres/polyhedra and orange spheres, respectively. Dashed black lines signify the cell boundaries.

exhibit a distorted rutile-type arrangement, characterized by their monoclinic  $P121/n1$  space group [114,115]. Most of the  $MF_3$  ( $M = \text{Ti, V, Cr, Fe, and Co}$ ) compositions crystallize in a rhombohedral structure within the  $R\bar{3}cR$  space group [116–120], with  $\text{NiF}_3$  adopting a similar rhombohedral structure within the  $R\bar{3}R$  space group [109].  $\text{MnF}_3$  exhibits a monoclinic crystal structure within the  $C12/c1$  space group, with Fig. 1 showing a  $2 \times 1 \times 1$  supercell to accommodate the A-type AFM ordering [121].  $MF_4$  compositions exhibit diverse crystal structures, such as orthorhombic ( $Pnma$  space group)  $\text{TiF}_4$  [122], monoclinic ( $P121/n1$ )  $\text{VF}_4$  [123], and tetragonal ( $P42/mnm$  and  $I41/a$ )  $\text{CrF}_4$  and  $\text{MnF}_4$  [124,125].

We initialized the magnetic configuration of each structure according to its known experimental ground state configuration, wherever possible [88,96,97,100–106,108,109], as listed in Table I and depicted in Fig. S2 [84]. The presence of the  $\pm$  sign or the AFM notation in Table I indicates antiferromagnetic configurations. In general, all AFM TMFs examined in this work have similar (G-type or  $\uparrow\downarrow\uparrow\downarrow$ ) ordering, with the exception of  $\text{MnF}_3$ , which exhibits an A-type ( $\uparrow\uparrow\downarrow\downarrow$ ) ordering [88]. Unlike other  $MF_3$ ,  $\text{NiF}_3$  is usually represented as a  $\text{Ni}[\text{NiF}_6]$  chemical formula to indicate the presence of Ni in the II and IV oxidation states. Notably, upon initialising the structure with both FM and AFM configurations, we obtained the FM configuration to be the ground state in  $\text{NiF}_3$  with the SCAN functional, where the Ni atoms exhibited both II and IV oxidation states, in agreement with experiment [109]. Subsequently, we initialized  $\text{NiF}_3$  in the FM configuration for all SCAN+ $U$  and  $r^2\text{SCAN}(+U)$  calculations.

The ground state magnetic configurations are not experimentally known for  $\text{TiF}_3$ ,  $\text{CrF}_4$ , and  $\text{MnF}_4$ . While  $\text{TiF}_3$  is known to be AFM [100], the specific configuration of mo-

ments is not known. Therefore, we considered the G-type AFM ordering for  $\text{TiF}_3$  as it is the only possible AFM arrangement within the two-Ti-atom conventional cell. Considering other complex AFM arrangements in  $\text{TiF}_3$  will require larger supercells and significant computational expense. In the cases of  $\text{CrF}_4$  and  $\text{MnF}_4$ , we considered the FM and all possible AFM configurations within the conventional cell and determined the ground state using the SCAN functional. Specifically, we considered FM + two AFM configurations and FM + five AFM orderings for  $\text{CrF}_4$  and  $\text{MnF}_4$ , respectively (see Fig. S3 [84]). Subsequently, we initialized  $\text{CrF}_4$  and  $\text{MnF}_4$  in the SCAN-calculated ground state magnetic configuration for all SCAN+ $U$  and  $r^2\text{SCAN}(+U)$  calculations.

### III. RESULTS

#### A. Fluorine binding

To examine whether  $\text{F}_2$  is under or overbound by SCAN and/or  $r^2\text{SCAN}$ , we evaluated the binding energy of the  $\text{F}_2$  molecule with both functionals. In the case of SCAN, we calculate a binding energy of  $-1.57$  eV, which is slightly lower but in close alignment with the experimental value of  $-1.64$  eV [94], indicating a marginal underestimation (by 3.9%). On the other hand, the  $r^2\text{SCAN}$ -calculated binding energy ( $-1.63$  eV) is in excellent agreement with the experimental value, indicating no errors arising from the electronic description of the  $\text{F}_2$  molecule. Thus, our binding energy calculations suggest that both functionals describe the  $\text{F}_2$  molecule with sufficient accuracy, and any errors in calculated fluorination enthalpies within TMFs should predominantly arise from SIEs caused by delocalized  $d$  electrons on the TM centers.

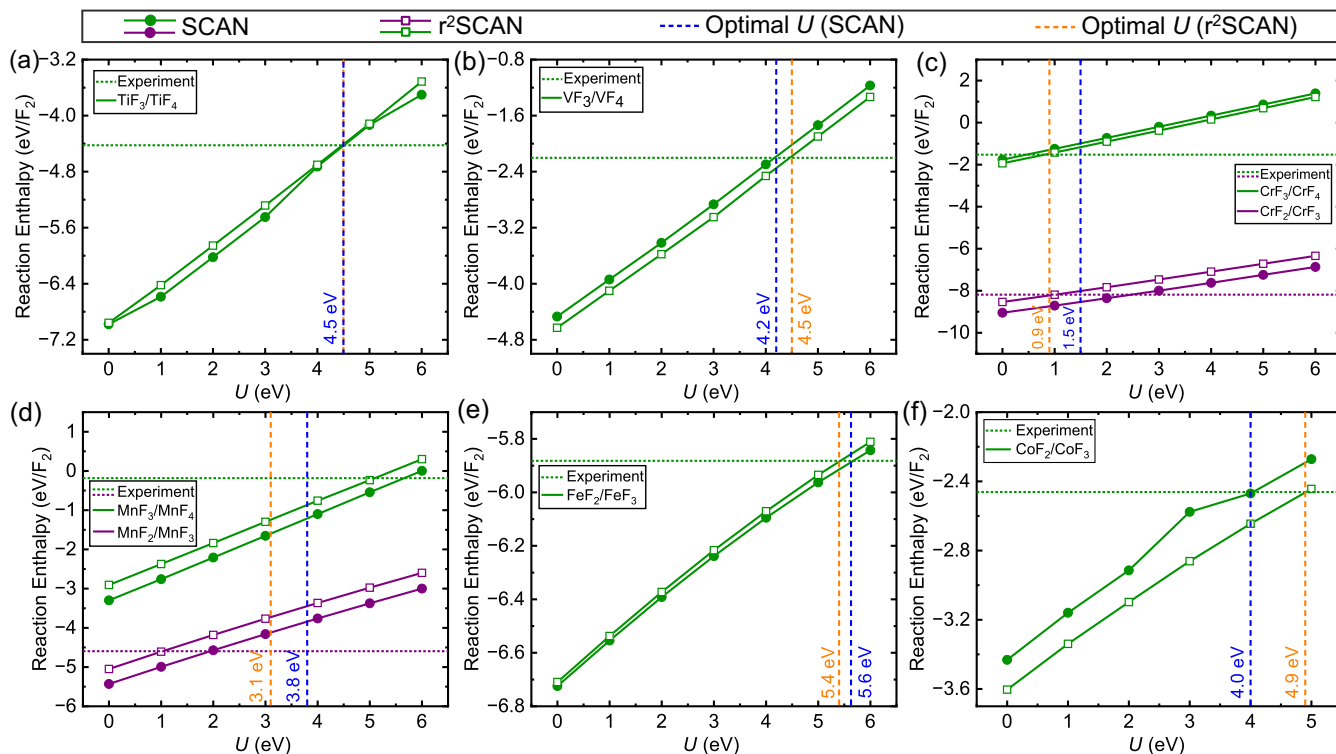


FIG. 2. Oxidation (or fluorination) reaction enthalpy (solid line) variation with increasing  $U$  within the SCAN+ $U$  and  $r^2$ SCAN+ $U$  functionals for (a) Ti, (b) V, (c) Cr, (d) Mn, (e) Fe, and (f) Co fluorides. For systems with multiple possible oxidation states (e.g., Cr and Mn), each reaction is represented by a different color. Horizontal dotted line of a given color in each panel reflects the experimental oxidation enthalpy for the reaction considered (at 298 K). Vertical blue and orange dashed lines indicate optimal  $U$  (magnitude is annotated as blue and orange text) for SCAN+ $U$  and  $r^2$ SCAN+ $U$  functional, respectively.

### B. Fluorination energetics of TMFs

Figure 2 displays the calculated fluorination (or oxidation) enthalpies of  $\text{Ti}^{+3}/\text{Ti}^{+4}$  (panel a),  $\text{V}^{+3}/\text{V}^{+4}$  (b),  $\text{Cr}^{+2}/\text{Cr}^{+3}/\text{Cr}^{+4}$  (c),  $\text{Mn}^{+2}/\text{Mn}^{+3}/\text{Mn}^{+4}$  (d),  $\text{Fe}^{+2}/\text{Fe}^{+3}$  (e), and  $\text{Co}^{+2}/\text{Co}^{+3}$  (f) as a function of  $U$  in SCAN+ $U$  (solid circles) and  $r^2$ SCAN+ $U$  (open squares) frameworks. Except for  $\text{Mn}^{+2}/\text{Mn}^{+3}$  and  $\text{Cr}^{+2}/\text{Cr}^{+3}$  (represented by purple lines and symbols) all fluorination reactions in Fig. 2 are indicated by green lines and symbols. The horizontal green and purple dotted lines indicate the experimental fluorination enthalpies (at 298 K) for the corresponding fluorination reactions. The optimal  $U$  in each panel, which minimizes the error between the calculated and experimental fluorination enthalpies, is represented by a vertical dashed blue line for SCAN+ $U$  and vertical dashed orange line for  $r^2$ SCAN+ $U$ , respectively.

Noticeably, the calculated fluorination enthalpies for most TMs evaluated using SCAN and  $r^2$ SCAN ( $U = 0$  eV) show significant discrepancies versus the corresponding experimental values. For example, the experimental fluorination enthalpy of  $\text{Ti}^{+3}/\text{Ti}^{+4}$  ( $-4.432$  eV/ $F_2$ ) is estimated to be more negative (i.e., magnitude is overestimated) by both SCAN ( $-6.98$  eV/ $F_2$ ) and  $r^2$ SCAN ( $-6.96$  eV/ $F_2$ ). Similarly, the experimental fluorination enthalpies (in eV/ $F_2$ ) of  $\text{V}^{+3}/\text{V}^{+4}$  ( $-2.20$ ),  $\text{Cr}^{+2}/\text{Cr}^{+3}$  ( $-8.18$ ),  $\text{Cr}^{+3}/\text{Cr}^{+4}$  ( $-1.52$ ),  $\text{Mn}^{+2}/\text{Mn}^{+3}$  ( $-4.60$ ),  $\text{Mn}^{+3}/\text{Mn}^{+4}$  ( $-0.18$ ),  $\text{Fe}^{+2}/\text{Fe}^{+3}$  ( $-5.88$ ), and  $\text{Co}^{+2}/\text{Co}^{+3}$  ( $-2.46$ ) are consistently overestimated by SCAN ( $-4.46$ ,  $-9.04$ ,  $-1.76$ ,  $-5.44$ ,  $-3.3$ ,  $-6.72$ ,

$-3.5$  eV/ $F_2$ , respectively) and  $r^2$ SCAN ( $-4.62$ ,  $-8.54$ ,  $-1.94$ ,  $-5.04$ ,  $-2.90$ ,  $-6.72$ ,  $-3.60$  eV/ $F_2$ , respectively). Thus, both SCAN and  $r^2$ SCAN overestimate experimental fluorination enthalpies for all TMs considered, which can be attributed to residual SIEs and erroneous description of the ground state electronic structures. Therefore, it is necessary to use the Hubbard  $U$ -corrected SCAN (SCAN+ $U$ ) or  $r^2$ SCAN ( $r^2$ SCAN+ $U$ ) frameworks to obtain more accurate estimations of TMF properties.

Given that the magnitude of  $U$  is not known *a priori*, we determine the optimal  $U$  for all 3d TMs based on the corresponding fluorination energies among the binary fluorides. For example, in Ti, we estimate an optimal  $U$  of 4.5 eV for both SCAN and  $r^2$ SCAN [Fig. 2(a)], which minimizes the error between experimental and calculated oxidation enthalpies for the  $\text{Ti}^{+3}/\text{Ti}^{+4}$  reaction. Similarly, we obtain an optimal  $U$  of 4.2, 1.5, 3.8, 5.6, and 4.0 eV for V, Cr, Mn, Fe, and Co, respectively, with SCAN, while the corresponding  $U$  values with  $r^2$ SCAN are 4.5, 0.9, 3.1, 5.4, and 4.9 eV [Figs. 2(b)–2(f)]. In the case of Mn, the optimal  $U$  of 3.8 eV with SCAN and 3.1 eV with  $r^2$ SCAN are obtained by averaging  $U$  for  $\text{MnF}_2 \rightarrow \text{MnF}_3$  (1.9 eV with SCAN, 1.0 eV with  $r^2$ SCAN) and  $\text{MnF}_3 \rightarrow \text{MnF}_4$  (5.6 eV, 5.1 eV) reactions (Fig. S1 [84]). Analogous averaging of  $U$  values for the  $\text{CrF}_2 \rightarrow \text{CrF}_3$  and  $\text{CrF}_3 \rightarrow \text{CrF}_4$  reactions is used to determine the optimal  $U$  for Cr with both SCAN and  $r^2$ SCAN.

Notably, the optimal  $U$  values obtained in the TMF chemical space are larger than the corresponding TMO chemical space [47], consistent with the higher degree of ionic bonding in fluorides than oxides, thereby requiring better electronic localization within the contracted  $3d$  orbitals. Note that higher degree of ionic bonding can also cause a larger degree of contraction of  $d$  orbitals, resulting in higher SIEs with semilocal functionals and a higher required  $U$  correction. Also, the nonmonotonic variation of optimal  $U$ , across the  $3d$  series, in  $r^2$ SCAN is similar to SCAN, indicating that the differences between these two functionals are marginal with respect to their accuracy in calculating redox enthalpies.

In the case of Ni and Cu fluorides, both metaGGA functionals underestimate and overestimate, respectively, the fluorination enthalpy compared to experimental values for the  $\text{Ni}^{+2}/\text{Ni}^{+3}$  and  $\text{Cu}^+/\text{Cu}^{+2}$  reactions (see Fig. S4 [84]). The overestimation of fluorination enthalpy for the  $\text{Cu}^+/\text{Cu}^{+2}$  reaction by both SCAN and  $r^2$ SCAN is similar to our observation in the  $\text{CuO}/\text{Cu}_2\text{O}$  system as well [47]. Moreover, the addition of  $U$  to both SCAN and  $r^2$ SCAN worsens the disparity between the calculated and experimental fluorination enthalpies for both Ni and Cu (Fig. S4 [84]), unlike the behavior of other TMs in Fig. 2.

We also explored adding a negative  $U$  parameter to the SCAN functional in Ni and Cu fluorides to see whether we can match the experimental fluorination enthalpy. Adding negative  $U$  is equivalent adding just a  $J$  parameter, which may facilitate electron delocalization, compared to the effect of adding a  $U$  that promotes electron localization. Notably, for Ni fluorides a  $U$  value of  $-2.7$  eV reproduces the experimental fluorination enthalpy as shown in Fig. S4(c) [84], but this value may lead to errors in other property predictions. In Cu fluorides, despite exploring a wide range of  $U$  from  $-15$  to  $6$  eV, the calculated values never match the experimental enthalpy, as depicted in Fig. S4(d) [84], suggesting broader limitations in the applicability of the DFT+ $U$  framework in Cu systems. Although we have explored adding negative  $U$  corrections to the SCAN functional in Ni and Cu fluorides, we expect similar trends to hold when such corrections are added to the  $r^2$ SCAN functional as well.

Note that in systems where a positive  $U$  correction does not yield better estimations of known properties, a shift towards the DFT+ $U$ + $V$  [126] framework, where the  $V$  parameter represents intersite interactions, may help. For example, instead of using a negative  $U$  value to open a band gap in InAs [70], the DFT+ $U$ + $V$  framework with a positive  $U$  as well as positive  $V$  can be used [127]. Using a positive  $U$  ensures that the physical purpose of the  $U$  parameter remains intact, i.e., localization of electrons. Thus, the DFT+ $U$ + $V$  framework may offer better accuracy in property predictions for Cu and Ni systems than the DFT+ $U$  method. Until the DFT+ $U$ + $V$  framework and suitable  $V$  values are widely available, we propose that the bare SCAN and  $r^2$ SCAN functionals be used in Ni and Cu fluorides.

### C. Linear response theory calculations

Note that the optimal  $U$  calculated using experimental enthalpies at 0 K (see Table S2 [84]) and 298 K, are similar ( $<0.5$  eV) or identical for Ti, Cr, Mn, and Co fluorides with

SCAN and  $r^2$ SCAN. Specifically, using 0 K experimental enthalpy data, the optimal  $U$  with SCAN ( $r^2$ SCAN) are 4.5, 1.7, 3.9, and 3.7 eV (4.5, 1.1, 3.2, and 5.2 eV) for Ti, Cr, Mn and Co, respectively (Table S2). These values are fairly similar to the corresponding optimal  $U$  derived using 298 K enthalpy data with SCAN ( $r^2$ SCAN), namely, 4.5, 1.5, 3.8, and 4.0 eV (4.5, 0.9, 3.1, and 4.9 eV; Fig. 2) for Ti, Cr, Mn, and Co, respectively.

However, the optimal  $U$  for V- and Fe-fluorides can be significantly different ( $>1$  eV), depending on whether 0 K or 298 K experimental enthalpies are considered. For instance, we obtain a  $U$  value of 3.0 eV with experimental data at 0 K and 4.2 eV with data at 298 K for V fluorides using SCAN, while the corresponding  $U$  values with  $r^2$ SCAN are 3.3 (0 K) and 4.5 eV (298 K). Similarly, using 0 K and 298 K experimental data yield  $U$  values of 3.6 (3.5) and 5.6 (5.4) eV, respectively, with SCAN ( $r^2$ SCAN) for Fe fluorides.

Given this ambiguity over experimental enthalpies in V and Fe fluorides, we use the linear response theory to obtain a  $U$  that is theory-derived and to provide a point of comparison to the experimental-derived  $U$  values. Additionally, we used linear response theory in Ni fluorides to verify the need for a  $U$  correction, since experimental data indicate that a  $U$  correction is not necessary for Ni, in contrast to observations in Ni oxides [47]. The NSCF or bare response and the SCF or interacting response with an applied potential ( $\alpha$ ) and the SCAN functional, for  $\text{VF}_3$ ,  $\text{VF}_4$ ,  $\text{FeF}_2$ ,  $\text{FeF}_3$ ,  $\text{NiF}_2$ , and  $\text{NiF}_3$  are plotted in Fig. 3. The NSCF and SCF responses are quantified as the number of electrons in the  $d$  orbitals ( $N_d$ ).

While the linear-response-theory-derived  $U$  for  $\text{VF}_3$  (with SCAN) is 8.7 eV [Fig. 3(a)], which is higher than that either of the experimental-derived  $U$  values (3.0–4.2 eV), the theory-derived  $U$  for  $\text{VF}_4$  is 4.2 eV [Fig. 3(b)], which matches the experimental-derived  $U$  using data at 298 K. Thus, the theory-derived  $U$  value increases significantly (by  $\sim 4.5$  eV) with lowering the oxidation state of V from +4 to +3.

Similarly, the theory-derived  $U$  of Fe in  $\text{FeF}_2$  and  $\text{FeF}_3$  are 16 eV and 6.1 eV [Figs. 3(c) and 3(d)], respectively, where the latter is similar to the experimental-derived  $U$  (5.6 eV), with the data at 298 K. As in V, the theory-derived  $U$  in Fe also increases significantly (by  $\sim 9.9$  eV) with a reduction in Fe oxidation state. In the case of Ni, theory yields  $U$  of 9.4 eV and 8.1 eV in  $\text{NiF}_2$  and  $\text{NiF}_3$  [Figs. 3(e) and 3(f)], respectively, significantly higher than the experimental-derived  $U$  of 0 eV. The variation in theory-derived  $U$  in Ni with reduction in Ni oxidation state is lower in Ni ( $\sim 1.3$  eV) compared to Fe and V, possibly because of the pairing of  $d$  electrons in several orbitals resulting in lower differences in the SIEs incurred between  $\text{Ni}^{+2}$  and  $\text{Ni}^{+3}$ . Nevertheless, the significant disparity between the experimental- and theory-derived  $U$  for Ni may be emblematic of general challenges within the DFT+ $U$  framework itself.

To check whether the range of  $\alpha$  values explored in Figure 3 is too large to ensure a linear response, we considered a smaller range of  $\alpha$ , i.e., between  $-0.05$  to  $0.05$  eV, in  $\text{FeF}_2$  and  $\text{VF}_3$  systems. As depicted in Fig. S17 [84], narrowing the  $\alpha$  range reduced the  $U$  value from 16 to 11.2 eV for  $\text{FeF}_2$ , while the  $U$  value increased from 8.7 to 9.3 eV for  $\text{VF}_3$ . However, the  $U$  values calculated over a narrower  $\alpha$  range for both  $\text{FeF}_2$

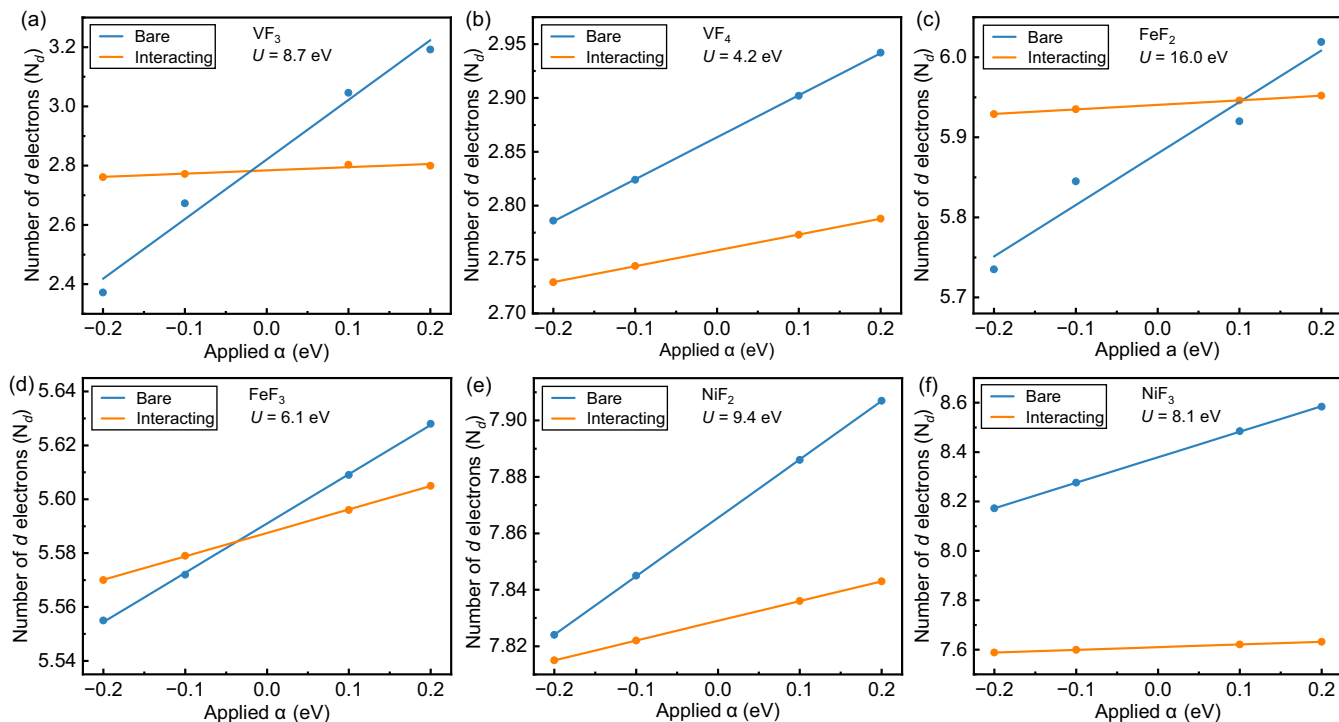


FIG. 3. Determination of Hubbard  $U$  using linear response theory and SCAN for (a)  $\text{VF}_3$ , (b)  $\text{VF}_4$ , (c)  $\text{FeF}_2$ , (d)  $\text{FeF}_3$ , (e)  $\text{NiF}_2$ , and (f)  $\text{NiF}_3$ . Each panel depicts the variation in the number of electrons ( $N_d$ ) in  $d$  orbitals of a single TM site as a function of the applied perturbation potential ( $\alpha$  in eV). The blue line represents data obtained from non-self-consistent field (NSCF) or “bare” calculations, while the orange line corresponds to SCF or “interacting” calculations. The magnitude of  $U$  is indicated as a text annotation in each panel.

and  $\text{VF}_3$  remain significantly higher (and unphysical) than the fitted  $U$  values of 5.6 and 4.2 eV for Fe and V fluorides, respectively.

Additionally, we computed a Hund’s  $J$  [63,128] parameter for  $\text{VF}_3$  to examine if adding an explicit  $J$  makes a tangible difference in the  $U$  correction estimated by linear response, following the procedure of Himmetoglu *et al.* [128]. Specifically, we calculated a  $J$  of 1.4 eV for  $\text{VF}_3$ , as shown in Fig. S18 [84]. However, the resultant effective Hubbard ( $U_{\text{eff}} = U - J = 9.3 \text{ eV} - 1.4 \text{ eV} = 7.9 \text{ eV}$ ) does remain significantly higher than the  $U_{\text{eff}}$  obtained using the experimental formation enthalpy (4.2 eV). Although we have performed linear response calculations with the SCAN functional, given the similarities in performance between SCAN and  $r^2\text{SCAN}$ , we believe that similar trends in theory-derived  $U$  values will be encountered with  $r^2\text{SCAN}$  as well.

Considering the substantial variation in theory-derived  $U$  across different oxidation states in V, Fe, and Ni, and the large unphysical values of  $U$  that we obtain for some oxidation states ( $>8 \text{ eV}$ ), we can conclude that linear response theory is currently not suitable for obtaining reliable  $U$  values for TMFs. Note that linear response theory has been known to provide larger-than-necessary  $U$  corrections in the TMO chemical space as well [62,73,129]. Given the unreliability of linear response theory, it does not provide a robust point of comparison for experimental-derived  $U$  values, particularly for the cases of V and Fe fluorides.

Nevertheless, we can use the following points to identify which experimental-derived  $U$  value is better for V and Fe: (1) Both SCAN and  $r^2\text{SCAN}$  exhibit the highest optimal  $U$  for

Fe in TMOs given that Fe has the largest number of unpaired electrons in its +3 oxidation state, which is also quite stable compared to its +2 state [47,57,58]. Also, both functionals display a lower optimal  $U$  in V and Cr compared to Ti in TMOs [47]. Given that fluorides are also ionically bonded compounds like oxides, we should expect similar trends to hold and the optimal  $U$  to hit its maximum for Fe. (2) We expect better localization of  $d$  electrons in fluorides compared to oxides since  $\text{F}^-$  leads to more ionic bonds than  $\text{O}^{2-}$ . Hence, optimal  $U$  values in fluorides should be larger than oxides. (3) The calculated lattice parameters, on-site magnetic moments, and band gaps should have good agreement with experiments (see subsections below, Tables S5 and S6, and Figs. S13 and S14 [84]). Thus, given the above considerations, we utilize the  $U$  calculated using thermochemical data at 298 K for all further calculations, and we believe that this  $U$  value is more reliable than the one calculated using extrapolated thermochemical data at 0 K.

#### D. Lattice volumes

The SCAN(+ $U$ ) and  $r^2\text{SCAN}$ (+ $U$ ) calculated lattice parameters for all TMFs considered are compiled in Table S3 [84]. Figure 4 displays a violin plot of the percentage difference in calculated and experimental lattice volumes, for all four frameworks. Positive (negative) differences between the calculated and experimental lattice volume indicate that the calculation underestimates (overestimates) with respect to the experiment. The embedded inner boxes within each violin encompass values ranging from the lower to the upper

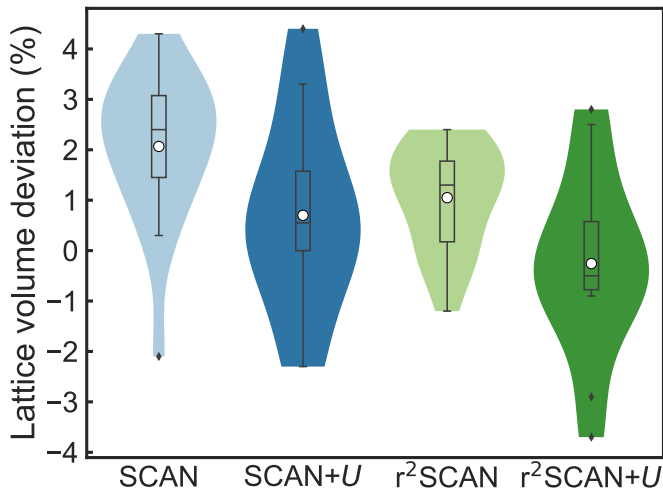


FIG. 4. Violin plot presenting the percentage error in the deviation of SCAN (light blue), SCAN+ $U$  (dark blue),  $r^2$ SCAN (light green), and  $r^2$ SCAN+ $U$  (dark green) calculated lattice volumes with respect to the corresponding experimental volumes for different TMFs. Positive (negative) values on the  $y$  axis indicate that the calculated volume is lower (higher) than the experimental value. The embedded inner boxes signify the lower to upper quartile range. Within each inner box, the mean and the median deviations are represented by the empty circle and the horizontal line, respectively. Black diamonds are outliers.

quartiles, with the black diamonds indicating outliers. Mean and median of the percentage error is shown as the empty circle and the horizontal black line, respectively, within the embedded inner box for each functional.

Overall, SCAN underestimates lattice volumes compared to experimental values, on average, with errors in the range of 0.3% to 4.3%, while the mean and median errors are 2.0% and 2.4%, respectively. The exception with SCAN is CuF, where SCAN overestimates the lattice volume by 2.1%. Compared to SCAN,  $r^2$ SCAN provides lower lattice volume deviations, on average, with the calculated volumes underestimating experiments in the range of 0.9–2.4%, with corresponding mean and median of 0.9% and 1.3%, respectively. Thus,  $r^2$ SCAN's lattice volume predictions are on average better than SCAN in TMFs, consistent with trends observed by Kingsbury *et al.* [46]. Note that there are several structures where  $r^2$ SCAN does overestimate experimental volumes, such as CrF<sub>3</sub> (0.1%), FeF<sub>3</sub> (0.5%), and CuF (1.2%), compared to only CuF with SCAN.

For several TMFs, adding the  $U$  correction with both SCAN and  $r^2$ SCAN enhances the calculated lattice volumes, thereby reducing the extent to which volumes are underestimated by the noncorrected functionals, resulting in lower mean and median errors. For instance, SCAN+ $U$  ( $r^2$ SCAN+ $U$ ) exhibits mean and median errors of 0.8% (−0.2%) and 1.1% (−0.5%), respectively, which are lower than the mean and median errors exhibited by SCAN ( $r^2$ SCAN). However, the range of errors observed in lattice volume calculations upon adding  $U$  corrections also increases for both functionals, due to the presence of outliers. For example, the errors in calculated volumes range from −2.3% to 3.3% with SCAN+ $U$ , and −0.9% to 2.5% for  $r^2$ SCAN+ $U$ ,

which are higher than the range of errors observed with SCAN (0.3 to 4.3%) and  $r^2$ SCAN (0.9 to 2.4%), respectively.

Notably,  $r^2$ SCAN+ $U$  exhibits a smaller range of errors and lower (in magnitude) mean and median errors than SCAN+ $U$ , similar to the comparison between  $r^2$ SCAN and SCAN. In terms of outliers, CoF<sub>3</sub> (error of 4.4%) is a significant outlier with SCAN+ $U$ , while CrF<sub>4</sub> (2.8%), TiF<sub>3</sub> (−2.9%), and VF<sub>3</sub> (−3.7%) are the primary outliers with  $r^2$ SCAN+ $U$ . Thus, the addition of Hubbard  $U$  to both SCAN and  $r^2$ SCAN leads to inconsistent improvements in the lattice parameter estimations compared to the noncorrected functionals. Nevertheless, the absolute magnitude of errors made by all functionals against experimental values are quite reasonable (<5% deviations), and the accuracy of one functional over another is marginal.

### E. On-site magnetic moments

Figure 5 depicts the experimental [88,101–108,110] and calculated on-site magnetic moments of the 3d TMs in the TMFs considered in this study, with the corresponding values also listed in Table S3 [84]. The magnetic moments in Fig. 5 are over a range of 0  $\mu_B$  (dark blue) to 5  $\mu_B$  (red). For fluorides without any experimental magnetic moment data, such as TiF<sub>3</sub>, CrF<sub>4</sub>, and NiF<sub>3</sub>, and for Ni and Cu fluorides that don't require a  $U$  correction, the lack of an experimental and/or calculated on-site magnetic moment is indicated by the hatched boxes in Fig. 5. Given the  $d^0$  and  $d^{10}$  electronic configurations on the Ti and Cu ions in TiF<sub>4</sub> and CuF, respectively, we have assigned the experimental on-site magnetic moments for these compounds to be 0. Note that the plotted on-site magnetic moments are averaged over all TMs present in a given structure. For AFM structures, we took the average of the absolute on-site magnetic moments on individual TMs.

Interestingly, the calculated on-site magnetic moments vary quite marginally across all functionals used within each TMF. For instance, the calculated on-site magnetic moments of TiF<sub>3</sub> (0.9  $\mu_B$ ), TiF<sub>4</sub> (0.0  $\mu_B$ ), VF<sub>4</sub> (1.0  $\mu_B$ ), CrF<sub>2</sub> (3.7  $\mu_B$ ), CrF<sub>3</sub> (2.8  $\mu_B$ ), CrF<sub>4</sub> (2.0  $\mu_B$ ), NiF<sub>2</sub> (1.7  $\mu_B$ ), NiF<sub>3</sub> (1.6  $\mu_B$ ), CuF (0.1  $\mu_B$ ), and CuF<sub>2</sub> (0.8  $\mu_B$ ) are identical for all XC frameworks. There are also structures where the calculated moments are identical or similar for SCAN and  $r^2$ SCAN, and/or for SCAN+ $U$  and  $r^2$ SCAN+ $U$ . For example, SCAN and  $r^2$ SCAN calculated magnetic moments of VF<sub>3</sub> (1.8  $\mu_B$ ), MnF<sub>2</sub> (4.6  $\mu_B$ ), FeF<sub>2</sub> (3.7  $\mu_B$ ), FeF<sub>3</sub> (4.2  $\mu_B$ ), CoF<sub>2</sub> (2.7  $\mu_B$ ), and CoF<sub>3</sub> (3.1  $\mu_B$ ) are identical, while for MnF<sub>3</sub> and MnF<sub>4</sub>, the difference is marginal (by  $\sim 0.1 \mu_B$ ). Similarly, SCAN+ $U$  and  $r^2$ SCAN+ $U$  calculated on-site magnetic moments are identical for VF<sub>3</sub> (1.9  $\mu_B$ ), MnF<sub>2</sub> (4.7  $\mu_B$ ), MnF<sub>3</sub> (3.8  $\mu_B$ ), MnF<sub>4</sub> (2.9  $\mu_B$ ), FeF<sub>2</sub> (3.8  $\mu_B$ ), and FeF<sub>3</sub> (4.5  $\mu_B$ ), with a marginal difference of 0.1  $\mu_B$  in CoF<sub>3</sub> ( $\sim 3.4 \mu_B$ ).

In terms of comparison to experimental data, the calculated on-site magnetic moments of most TMFs is in good agreement with experimental values, across the four XC frameworks, with computed values marginally underestimating experiments. As an exception, the calculated moments of MnF<sub>4</sub> (2.6–2.9  $\mu_B$ ) and CoF<sub>4</sub> (3.1–3.4  $\mu_B$ ) are significantly less than the experimental value of 3.9  $\mu_B$  and 4.4  $\mu_B$ , respectively, suggesting that all four XC frameworks favor a different spin configuration of Mn and Co as the electronic ground states compared to the experimental observations. Overall,



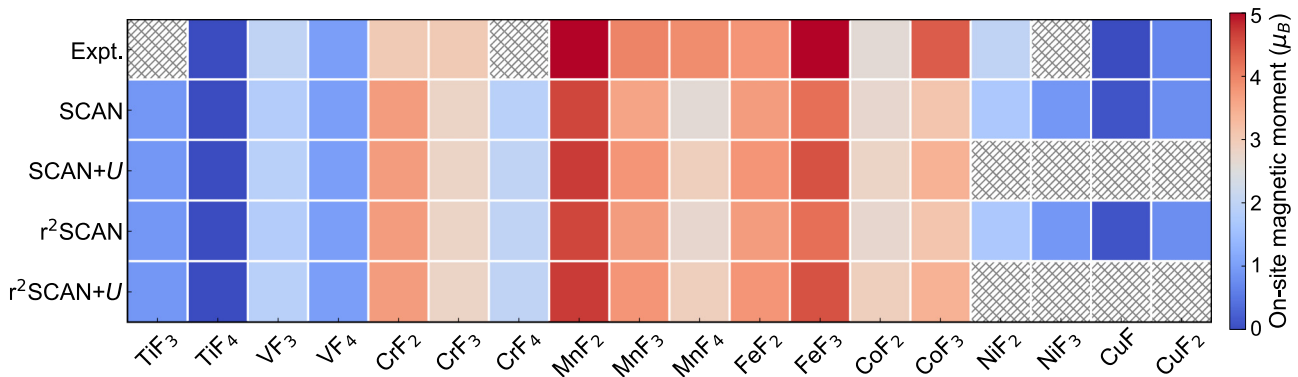


FIG. 5. On-site magnetic moments (in units of  $\mu_B$ ) of 3d TM in fluoride frameworks. Top (or first) row is experimental data, while second to fifth rows are calculated data, using SCAN (second), SCAN+ $U$  (third),  $r^2$ SCAN (fourth), and  $r^2$ SCAN+ $U$  (fifth). Hatched squares in the first row indicate absence of experimental data, while those in third and fifth rows indicate absence of SCAN+ $U$  and  $r^2$ SCAN+ $U$  values, since a  $U$  correction is not required for Ni and Cu fluorides.

the predictions of on-site magnetic moments do not change significantly ( $<0.3 \mu_B$ ) across the four XC frameworks for all the TMFs considered, highlighting similar levels of accuracy in predicting magnetic moments by all four XC frameworks compared to experiments.

#### F. Band gaps

To check the performance of the XC frameworks in predicting electronic properties, we calculated the electronic DOS for all the TMFs considered. All calculated band gaps are compiled in Figs. S5–S12 [84], with the corresponding band gap values listed in Table S3 [84]. Note that experimental measurements of band gaps, either via optical or photoemission/inverse photoemission spectroscopy, in binary TMFs are quite scarce. However, the colors of the powdered samples of all considered TMFs have been documented in literature [130–132]. Given the relationship between band gap and the color of a given compound [133], we approximated the experimental band gaps of all TMFs and used these for a qualitative comparison with the calculated band gaps.

The approximate experimental band gaps of TMFs are indicated by purple diamonds in Fig. 6(a), while the background indicates the visual spectrum (1.6–3.2 eV). We assumed all black (white) powder colored samples to exhibit low (high) band gap, i.e.,  $<1.6$  eV ( $>3.2$  eV) eV, and specifically assigned a band gap value of 1 (3.5) eV. Note that all TMFs considered, except NiF<sub>3</sub>, TiF<sub>4</sub>, FeF<sub>2</sub>, CuF, and CuF<sub>2</sub>, should have a band gap in the 1.6–3.2 eV range, given their observed powder colors. Thus, except NiF<sub>3</sub> (which is a black powder), all TMFs considered are expected to be semiconductors or insulators. The literature data on the colors and our numerically approximated band gaps are tabulated in Table S4 [84].

The calculated band gaps of the TMFs, using SCAN (blue circles), SCAN+ $U$  (green crosses),  $r^2$ SCAN (orange squares), and  $r^2$ SCAN+ $U$  (purple pluses), are displayed in Fig. 6(b). The band gap of SCAN+ $U$  and  $r^2$ SCAN+ $U$  for Ni and Cu fluorides are not included, as the addition of  $U$  is not required. Importantly, the SCAN and  $r^2$ SCAN calculated band gaps are quite similar for several TMFs ( $<1.1$  eV deviation), and are in the range of  $\sim 0$ –2.8 eV, except for TiF<sub>4</sub> with a significantly higher band gap of  $\sim 4.4$  eV.

The band gaps of all TMFs, calculated using SCAN+ $U$  ( $r^2$ SCAN+ $U$ ) lie within a range of  $\sim 2.2$ –4.7 eV ( $\sim 1.8$ –4.7 eV), except the low band gap of CrF<sub>4</sub> ( $\sim 0.3$  eV with SCAN+ $U$  and  $\sim 0.4$  eV with  $r^2$ SCAN+ $U$ ). The trends in band gap estimates are quite similar among SCAN+ $U$  and  $r^2$ SCAN+ $U$ , with deviations  $<1.3$  eV, similar to the observed trends among SCAN and  $r^2$ SCAN calculations. Notably, upon  $U$  addition, the calculated band gaps of TMFs significantly increased compared to the corresponding non- $U$ -corrected versions, consistent with observations in other chemistries [47,57,58,134–136].

Clearly, the estimated empirical band gap of most TMFs tend to fall within the range between the (underestimated) predictions of SCAN/ $r^2$ SCAN and the (overestimated) predictions of SCAN+ $U$ / $r^2$ SCAN+ $U$ , as illustrated in Fig. 6. We have also plotted a heatmap of the difference between experimental and calculated band gaps in Fig. S15 [84]. Specifically, we find that both SCAN and  $r^2$ SCAN underestimate the gap of several compounds, namely, TiF<sub>3</sub>, VF<sub>3</sub>, VF<sub>4</sub>, CrF<sub>4</sub>, FeF<sub>2</sub>, CuF, and CuF<sub>2</sub>, with deviations from empirical estimates exceeding  $\sim 1.0$  eV. MnF<sub>2</sub> is an exception to this trend, as its band gap is overestimated (by  $\sim 1.0$  eV) by both SCAN and  $r^2$ SCAN. In some TMFs, both SCAN and  $r^2$ SCAN yield accurate gaps (with marginal underestimation), as in TiF<sub>4</sub>, CrF<sub>3</sub>, MnF<sub>3</sub>, MnF<sub>4</sub>, FeF<sub>3</sub>, CoF<sub>2</sub>, NiF<sub>2</sub>, and NiF<sub>3</sub>, with deviations  $<0.6$  eV from empirical estimates.

In several structures, the band gap calculated with the  $U$ -corrected framework is significantly higher than the empirical estimates, which is unusual for a ground state DFT+ $U$  theory. For example, both SCAN+ $U$  and  $r^2$ SCAN+ $U$  overestimate the gap (by  $\sim 1.3$  eV) in VF<sub>3</sub>, VF<sub>4</sub>, MnF<sub>2</sub>, FeF<sub>3</sub>, CoF<sub>2</sub>, and CoF<sub>3</sub>. CrF<sub>4</sub> is an exception in both  $U$  corrected frameworks, given the significantly underestimated gap (by  $\sim 1.9$  eV). In some structures, both SCAN+ $U$  and  $r^2$ SCAN+ $U$  demonstrate reasonable accuracy, with marginal overestimation, in predicting gaps, including TiF<sub>3</sub>, TiF<sub>4</sub>, CrF<sub>2</sub>, CrF<sub>3</sub>, MnF<sub>3</sub>, MnF<sub>4</sub>, and FeF<sub>2</sub>, where deviations from empirical values are  $<\sim 0.6$  eV.

Given the scarcity of experimentally measured band gaps in TMFs, it remains challenging to definitively declare one functional as more accurate than the other, emphasizing the need for additional experimental data for a comprehensive

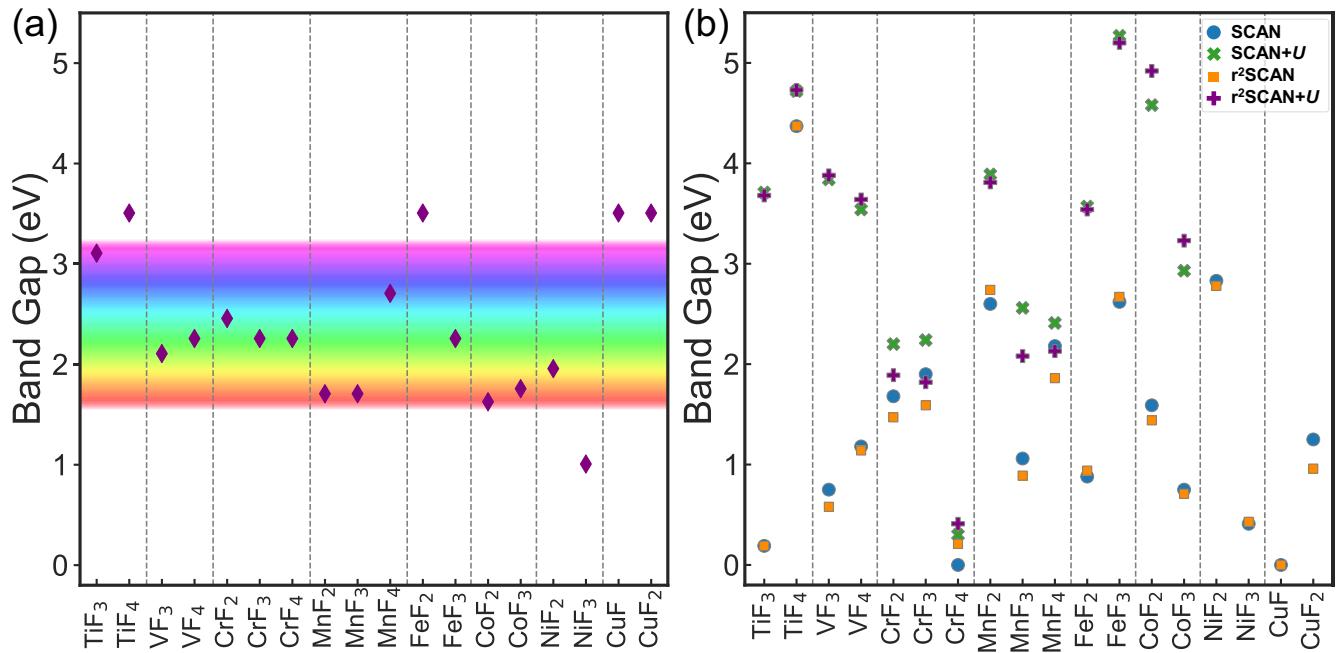


FIG. 6. (a) The estimated experimental band gap (purple diamond symbol) of various transition metal fluorides, based on their observed powder colors. The visible light spectrum (1.6–3.2 eV) is highlighted. A material with black (white) powder color is categorized as having a low band gap or metallic (high band gap or insulating) character, with band gap of  $<1.6$  eV ( $>3.2$  eV). (b) Schematic showing the calculated band gaps of TMFs using SCAN (blue symbols), SCAN+ $U$  (green),  $r^2$ SCAN (orange), and  $r^2$ SCAN+ $U$  (purple) frameworks.

assessment. Nevertheless, we compare the band gap calculated using SCAN(+ $U$ ) and  $r^2$ SCAN(+ $U$ ) frameworks with values from the HSE06 hybrid functional, given that hybrid functionals typically yield more accurate band gap predictions compared to DFT/DFT+ $U$  methods. While we calculated the HSE06 band gap of a few TMFs (TiF<sub>3</sub>, FeF<sub>2</sub>, and CoF<sub>2</sub>, DOS plots compiled in Fig. S19 [84]), we also used the reported HSE06 gaps by Mattsson and Paulus [137] in several TMFs for our comparison (see Table S6 [84]). Importantly, we find DFT+ $U$  band gaps to be in better alignment with HSE06 gaps compared to the non- $U$ -corrected functionals. For instance, SCAN+ $U$  ( $r^2$ SCAN+ $U$ ) gaps of 3.71 eV (3.68 eV) in TiF<sub>3</sub>, 3.57 (3.54) in FeF<sub>2</sub>, and 4.58 (4.92) in CoF<sub>2</sub> are closer to the corresponding HSE06 gaps of 2.54, 3.23, and 4.48, compared to SCAN ( $r^2$ SCAN) values of 0.19 (0.19), 0.88 (0.94), and 1.59 (1.44). We observe similar trends among the other TMFs listed in Table S6 [84]. Thus, we find the  $U$  correction to yield better band gap predictions with reference to HSE06 gaps compared to the bare functional, and we recommend the usage of  $U$ -corrected functionals for further band gap predictions in TMFs.

### G. Transferability check

It is important to verify the transferability of the optimal  $U$  determined using experimental data in binary systems to other binary or higher-component fluorides that were not taken into account during the determination of the optimal  $U$ . However, the lack of reliable experimental data in higher-component fluorides, except the case of Fe fluorides, provides a significant challenge in our efforts to investigate the transferability of  $U$  values. Consequently, we primarily focus on checking the transferability of the optimal  $U$  for Fe in Fe

fluorides. We utilize the experimentally measured topotactic Na (de)intercalation voltage ( $\sim 3.2$  V vs Na [138]) from NaFeF<sub>3</sub>, i.e., for the full extraction of Na, or NaFeF<sub>3</sub>  $\rightarrow$  Na + FeF<sub>3</sub>, as a point of comparison with calculated values. Structure of NaFeF<sub>3</sub> is displayed in Fig. S16 [84]. A description of calculating the average voltage from experimental enthalpies is given in the SM.

Importantly, the calculated enthalpy for the Na + FeF<sub>3</sub>  $\rightarrow$  NaFeF<sub>3</sub> with both SCAN and  $r^2$ SCAN is  $-2.8$  eV. This reaction enthalpy is equivalent to an average Na (de)intercalation voltage of 2.8 V vs Na, which is  $\sim 13\%$  lower than the experimental value. Remarkably, the average Na (de)intercalation voltage calculated with SCAN+ $U$ / $r^2$ SCAN+ $U$ , with our optimal  $U$  values, is 3.1 V, in excellent agreement with the experimental voltage. Thus, we believe that our optimal  $U$  value, especially in the case of Fe, should be suitable in modeling redox reactions across other Fe fluorides.

Demov *et al.* [138] measured voltages for partial extraction of Na (from  $x = 1$ ) in Na <sub>$x$</sub> MnF<sub>3</sub>, Na <sub>$x$</sub> CoF<sub>3</sub>, and Na <sub>$x$</sub> NiF<sub>3</sub>, all of which adopt structures similar to NaFeF<sub>3</sub>. Partial desodiation in the Mn, Co, and Ni fluorides also caused the formation of some impurity phases. Since modeling partial Na extraction will require considering various Na-vacancy configurations, and modeling impurities is not a trivial task computationally, we are unable to rigorously validate the measured partial desodiation voltages from experiment. However, we have calculated the average (de)intercalation voltage of Na, over the entire Na composition range (i.e.,  $0 \leq x \leq 1$ ), and over a partial composition range ( $0.75 \leq x \leq 1$ ) in the Mn, Co, and Ni fluorides with all four XC frameworks. The calculated voltages are compiled in Table II.

TABLE II. Calculated average voltages using SCAN, SCAN+ $U$ ,  $r^2$ SCAN, and  $r^2$ SCAN+ $U$  in Mn, Fe, Co, and Ni fluorides. Expt. indicates the experimental voltage measured in the  $\text{Na}_x\text{FeF}_3$  system ( $0 \leq x \leq 1$ ) [138].  $V'$  denotes the voltage calculated at a composition between  $\text{Na}_{0.75}\text{MF}_3$  and  $\text{NaMF}_3$  ( $M = \text{Mn, Co, and Ni}$ ), or for partial Na extraction.  $V''$  represents voltage calculated between compositions of  $\text{MF}_3$  and  $\text{NaMF}_3$  ( $M = \text{Mn, Fe, Co, and Ni}$ ), or for full Na extraction.

Compositions		Voltage (V)	
(Space group)	Source	$V'$	$V''$
$\text{Na}_x\text{MnF}_3$ ( $Pnma$ )	SCAN	2.8	3.2
	SCAN+ $U$	4.0	4.1
	$r^2$ SCAN	2.3	2.7
	$r^2$ SCAN+ $U$	3.3	3.5
$\text{Na}_x\text{FeF}_3$ ( $Pnma$ )	Expt.		3.2
	SCAN		2.8
	SCAN+ $U$		3.1
	$r^2$ SCAN		2.8
	$r^2$ SCAN+ $U$		3.1
$\text{Na}_x\text{CoF}_3$ ( $Pnma$ )	SCAN	4.1	4.5
	SCAN+ $U$	5.0	5.0
	$r^2$ SCAN	3.2	3.8
	$r^2$ SCAN+ $U$	4.3	4.3
$\text{Na}_x\text{NiF}_3$ ( $Pnma$ )	SCAN	4.9	5.1
	$r^2$ SCAN	4.2	4.5

From the calculated trends in voltages, we suspect that  $r^2$ SCAN+ $U$  can yield better accuracy than the other XC frameworks for the following reasons. First, SCAN+ $U$ , and also SCAN to an extent, has been shown to overestimate intercalation voltages in oxides [59], and we can expect similar behavior to hold for fluorides. Second, while intercalation voltages, across the entire Na content, are expected to increase from Fe to Co, a  $\sim 2$  V increase predicted by SCAN(+ $U$ ) is likely not physical.

Although there are no tabulated/reported experimental thermochemical data for benchmarking, we computed 0 K convex hulls (or 0 K phase diagrams) for select ternary fluoride systems as additional benchmarking. Specifically, we calculated the energy above the convex hull ( $E^{\text{hull}}$ ) to assess the role of  $U$  in predicting the stability (or instability) of compounds that were not considered in determining the optimal  $U$  correction. Thus, we calculated the convex hulls for Na-V-F, Na-Cr-F, Na-Mn-F, and Na-Fe-F ternary chemical spaces using SCAN and compared them to the corresponding SCAN+ $U$  hulls. Our calculated  $E^{\text{hull}}$  values are presented as bar charts in Fig. 7 and the 0 K convex hulls are depicted in Figs. S22 and S23 [84]. Although we haven't computed the  $r^2$ SCAN(+ $U$ ) hulls for the above ternary chemical spaces, we expect the trends to be similar to SCAN(+ $U$ ) calculations.

In ternary Na-V-F [Fig. 7(a)], SCAN predicts  $\text{Na}_3\text{VF}_6$  and  $\text{NaVF}_4$  to lie on the convex hull (i.e.,  $E^{\text{hull}} = 0$  meV/atom) indicating their thermodynamic stability, while  $\text{NaVF}_3$  lies above the hull ( $E^{\text{hull}} = 92$  meV/atom). SCAN+ $U$  exhibits similar trends as SCAN, predicting both  $\text{Na}_3\text{VF}_6$  and  $\text{NaVF}_4$  to be stable, and  $\text{NaVF}_3$  to be unstable with a slightly higher  $E^{\text{hull}} = 108$  meV/atom than SCAN. The comparison between

SCAN and SCAN+ $U$  is fairly similar in the Na-Cr-F chemical space as well [Fig. 7(b)]. For example, both SCAN and SCAN+ $U$  predict  $\text{Na}_3\text{CrF}_6$ ,  $\text{NaCrF}_4$ , and  $\text{NaCrF}_6$  to be stable, and  $\text{NaCrF}_3$  and  $\text{Na}_5\text{Cr}_3\text{F}_{14}$  to be unstable/metastable, with SCAN+ $U$   $E^{\text{hull}}$  values of the unstable/metastable compounds being marginally lower than SCAN values.

We observe minor qualitative differences in stability estimations between SCAN and SCAN+ $U$  in the Na-Mn-F and Na-Fe-F chemical spaces. For example, SCAN+ $U$  predicts  $\text{NaMn}_3\text{F}_{10}$  to be metastable ( $E^{\text{hull}} = 5$  meV/atom), while SCAN predicts the compound to be stable. Similarly, SCAN+ $U$  predicts  $\text{Na}_2\text{Fe}_2\text{F}_7$  to be metastable ( $E^{\text{hull}} = 19$  meV/atom), in contrast to SCAN's prediction of the framework to be stable. Note that in both  $\text{NaMn}_3\text{F}_{10}$  and  $\text{Na}_2\text{Fe}_2\text{F}_7$  instances, the  $E^{\text{hull}}$  predictions of SCAN+ $U$  lie within the typical stability threshold of 50 meV/atom that is used to estimate synthesizability of compounds [139]. Thus, the predictions of SCAN+ $U$  of metastability of  $\text{NaMn}_3\text{F}_{10}$  and  $\text{Na}_2\text{Fe}_2\text{F}_7$  are still consistent with experiments, since these compounds have been successfully synthesized [12,140].

On the other hand, SCAN's estimated  $E^{\text{hull}}$  in  $\text{NaFeF}_3$  (76 meV/atom) is well above the stability threshold of 50 meV/atom, while SCAN+ $U$  predicts a significantly lower  $E^{\text{hull}}$  of 26 meV/atom. Given that  $\text{NaFeF}_3$  is a well-known perovskite that can be synthesized using low-temperature wet-chemistry techniques [141] the expectation is that  $\text{NaFeF}_3$  is either on the hull (stable) or marginally off the hull (metastable). Thus, SCAN+ $U$ 's calculated  $E^{\text{hull}}$  is in better agreement with experimental observation in  $\text{NaFeF}_3$  than SCAN. In summary, we observe SCAN and SCAN+ $U$  to provide similar 0 K stability estimations across ternary fluorides, with SCAN+ $U$  being marginally in better agreement with experimental observations of synthesizable phases than SCAN.

#### IV. DISCUSSION

In this work, we have evaluated the accuracy of metaGGA (i.e., SCAN and  $r^2$ SCAN) functionals in describing the redox thermodynamics, lattice parameters, on-site magnetic moments, and band gaps of TMFs. While both SCAN and  $r^2$ SCAN don't exhibit a significant error in the binding of  $\text{F}_2$  molecule, we found both functionals to exhibit significant errors in fluorination reaction enthalpies compared to experiments (Fig. 2). Such errors in fluorination (i.e., oxidation) enthalpies can be attributed to SIEs of the  $3d$  electrons, necessitating the addition of  $U$  corrections to both functionals. Subsequently, we determined optimal  $U$  values based on experimental fluorination enthalpies for both SCAN and  $r^2$ SCAN. Importantly, we found marginal changes in lattice parameter and on-site magnetic moment predictions, while band gaps increased significantly upon adding the  $U$  correction to both SCAN and  $r^2$ SCAN (Figs. 4, 5, and 6 and Table S3 [84]). Finally, we looked at predictions of average Na intercalation voltages in ternary fluorides as transferability checks of our optimal  $U$  values in Mn, Fe, Co, and Ni systems (Table II).

Based on experimental enthalpies, we obtained an optimal  $U$  of 4.5 (Ti), 4.2 (V), 1.5 (Cr), 3.8 (Mn), 5.6 (Fe), 4.0 eV (Co) with SCAN+ $U$ , and 4.5 (Ti), 4.5 (V), 0.9 (Cr), 3.1 (Mn), 5.4

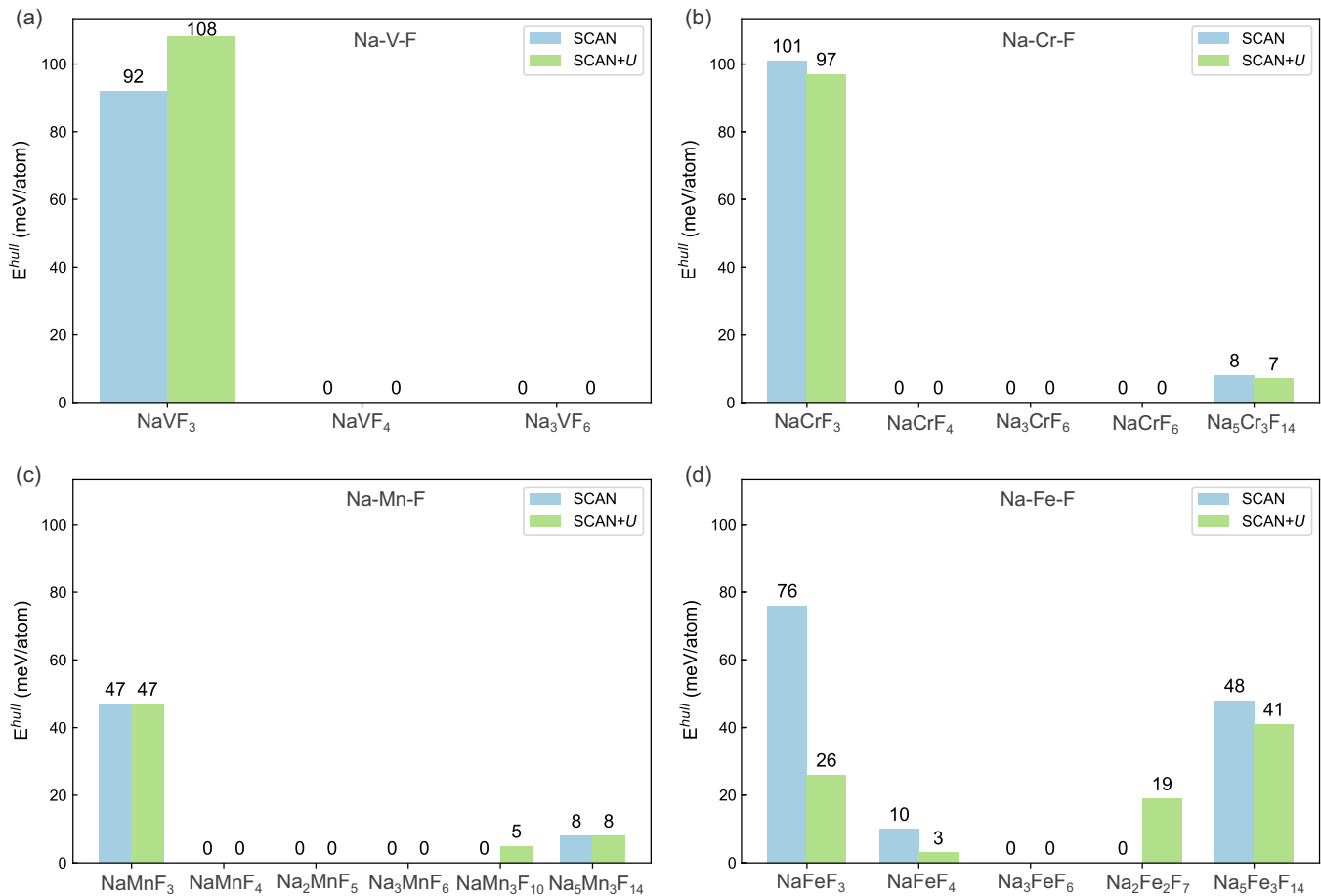


FIG. 7. Calculated  $E^{\text{hull}}$  for (a) Na-V-F, (b) Na-Cr-F, (c) Na-Mn-F, and (d) Na-Fe-F ternary fluorides. Blue and green bars represent SCAN and SCAN+ $U$  calculated values, which are presented as text annotations.

(Fe), 4.9 eV (Co) with  $r^2$ SCAN+ $U$ . Also, we determined that the  $U$  correction is not required for Ni and Cu fluorides, based on the (dis)agreement with experimental enthalpies. Notably, we did not obtain physically reasonable  $U$  values, particularly for the lower oxidation states, in V, Fe, and Ni fluorides using linear response theory (Fig. 3). Such unphysical  $U$  values indicate potential limitations in the applicability of the linear response theory with metaGGA functionals. Note that there are other ways of reducing SIEs in semilocal functionals, such as the DFT+ $U$ + $V$  framework [70,127,142–144], which require more tunable parameters that are not known *a priori* compared to the DFT+ $U$  framework.

Optimal  $U$  values in this work are nominally higher than the reported values derived from oxidation enthalpies for oxides [47,57,58]. This is expected given that fluorides are more ionic than oxides, resulting in more localized  $d$  electrons, thus making fluorides more susceptible to SIEs. However, the exception to this trend is Ni, where we do not observe the need for a  $U$  correction using redox enthalpies (Fig. S4). One reason could be the low band gap of  $\text{NiF}_3$  (black powder color experimentally), giving rise to an electronic ground state that has delocalized  $d$  electrons, which is better described by SCAN and  $r^2$ SCAN. Another possibility is a one-off cancellation of SIEs for both SCAN and  $r^2$ SCAN while taking energy differences between  $\text{NiF}_2$  and  $\text{NiF}_3$ . Nevertheless,

more experimental data, both thermochemical and electronic, are required to fully understand the source of this discrepancy.

For lattice volume and on-site magnetic moment predictions, there is practically no difference between Hubbard  $U$  corrected and noncorrected functionals, with both frameworks demonstrating good agreement with available experimental data. On the surface, this may give an indication that the residual SIEs don't really impact property predictions in the noncorrected functionals. However, the significant variation in the redox enthalpies indicates that even marginal changes in the electronic structure or geometry can have a significant impact in the redox behavior, in the TMF chemical space. With respect to magnetic moments,  $\text{MnF}_4$  is an exception, where the experimental magnetic moment of  $3.85 \mu_B$  significantly deviates from our computed on-site magnetic moments, in the range of  $2.6$ – $2.9 \mu_B$ , as presented in Fig. 5. The observed discrepancy may arise from uncertainties in the crystal structure of  $\text{MnF}_4$ , with our ground state structure potentially differing from the experimentally reported amorphous phase [104]. Given that  $\text{Mn}^{+4}$  theoretically has a maximum of three unpaired  $d$  electrons in its high spin state, corresponding to an ideal magnetic moment of  $\sim 3 \mu_B$ , it is unlikely for  $\text{Mn}^{+4}$  to exhibit an on-site magnetic moment exceeding  $3 \mu_B$ , unless significant reduction of  $\text{Mn}^{+4}$  occurs in a given structure.

The lack of reliable experimental data (and/or higher-order computational data), specifically thermochemical data, makes

comparisons with theoretical predictions difficult. For example, a cursory usage of thermochemical data given by Aykol and Wolverton [98] and tabulated in JANAF [92] or Barin [94] tables can give rise to dramatically different  $U$  values. This is at least the case for V and Fe fluorides, where we obtain significantly different  $U$  based on thermochemical data at 0 K and 298 K (Table S2 [84]). The discrepancies observed in the experimental data between 0 K and 298 K may be attributed to erroneous measurement at 298 K, spurious extrapolation of data to 0 K, and/or the occurrence of an unreported phase transitions in the bulk fluorides.

Similarly, it is hard to benchmark the band gaps in TMFs since robust measurements are not available. Note that colors of powdered samples can also be influenced by defects present in the sample—hence any band gap estimate can represent a significant approximation. This may be a source of error for cases where experimental band gaps (based on colors) do not even align qualitatively with computed band gaps (e.g., CuF, CuF<sub>2</sub>, and CrF<sub>4</sub>). Thus, more experimental data are required to increase confidence in theoretical predictions. While our DFT calculations provide a qualitative assessment of band gaps, it is important to recognize that DFT, even at the hybrid functional level, is not inherently designed to accurately predict band gaps, since band gaps are an excited-state property and DFT is a ground state theory. An alternative is to employ computationally expensive but accurate techniques, such as GW calculations [68,145,146], to get an estimate of band gaps and examine their comparison with DFT+ $U$  values.

To obtain a qualitative understanding of the change in the ground state electronic structure with  $U$  addition, we computed the difference in charge densities between SCAN and SCAN+ $U$  calculations for FeF<sub>2</sub>, as depicted in Fig. S20 [84]. We used the SCAN relaxed structure of FeF<sub>2</sub> to calculate the charge density difference. Notably, the presence of a "negative" charge density difference (depicted by the yellow isosurface in Fig. S20) surrounding the TM indicates a larger localization of electrons around the TM in the SCAN+ $U$  calculation compared to SCAN. Thus, adding the  $U$  correction is indeed effective in forcing electron localization around the TM in TMFs.

Furthermore, fluorides are expected to exhibit a higher degree of electron localization around the TM centers than their oxide counterparts, due to the higher electronegativity of F<sup>-</sup> and the associated higher ionicity of the bonds that are formed. The higher degree of localization should be captured by SCAN+ $U$  to validate the use of the  $U$  correction. To examine this, we calculated the charge density difference in select TMF-TMO pairs, i.e., TiF<sub>4</sub> – TiO<sub>2</sub> and MnF<sub>4</sub> – MnO<sub>2</sub>, where the TMs exhibit identical (+4) oxidation states. Specifically, we subtracted the charge density of SCAN+ $U$  from SCAN to evaluate the degree of electron localization within the TMFs and compared this to the analogous degree of localization (from charge density differences) in the corresponding oxides, as illustrated in Fig. S21 [84]. Remarkably, the electron density localization is much pronounced in TiF<sub>4</sub> and MnF<sub>4</sub> compared to TiO<sub>2</sub> and MnO<sub>2</sub>, respectively, in line with chemical intuition. This indicates the efficacy of  $U$  correction in describing the underlying electronic structure of TMFs, which leads to better material property predictions.

Finally, we note that the optimal  $U$  corrections obtained for TMFs in this work are indeed different from those for TMOs, using both SCAN and r<sup>2</sup>SCAN [47], which is inline with previous studies that have reported  $U$  values that are dependent on the local coordination environment of TMs [98]. While the requirement of different  $U$  values for oxides and fluorides is unfortunate, the corresponding optimal  $U$  values are indeed required for robust property predictions. Thus, to develop a unified theoretical framework to model systems that have mixed anionic coordination environment (e.g., oxyfluorides, where both TM-O and TM-F bonds are present), correction/mixing schemes that facilitate the comparison of energies calculated using different  $U$  values need to be developed. Note that correction/mixing schemes have been developed for GGA/GGA+ $U$  functionals [73] and in combining r<sup>2</sup>SCAN E<sup>hull</sup> with GGA/GGA+ $U$  calculated values, [147], which provide qualitative direction to develop similar schemes with either SCAN/SCAN+ $U$  or r<sup>2</sup>SCAN/r<sup>2</sup>SCAN+ $U$ .

## V. CONCLUSION

TMFs, which have a wide range of applications including energy storage, catalysis, and magnetic devices, are highly correlated electronic systems, which are susceptible to SIEs when described using semilocal metaGGA functionals, such as SCAN and r<sup>2</sup>SCAN. Hence, we have systematically examined the accuracy of SCAN and r<sup>2</sup>SCAN functionals in estimating the redox enthalpies, lattice parameters, on-site magnetic moments, and band gaps of binary TMFs. Importantly, we revealed that metaGGA functionals do overestimate (i.e., more negative) fluorination enthalpies among binary TMFs, which can be primarily attributed to the SIEs among  $d$  electrons since both SCAN and r<sup>2</sup>SCAN bind F<sub>2</sub> precisely. Given that SIEs can be mitigated by the addition of a Hubbard  $U$  correction, we subsequently derived optimal  $U$  values for different TMs based on experimental fluorination enthalpies. While the  $U$ -corrected frameworks increased the calculated band gaps significantly compared to the non- $U$ -corrected functionals (resulting in better alignment with band gaps calculated using a hybrid functional), the lattice parameters and on-site magnetic moments were only marginally different. Also, we examined the transferability of the optimal  $U$  values determined in this work via 0 K convex hull calculation of ternary fluorides (Na-M-F, M = V, Cr, Mn, and Fe) and comparison with available Na-intercalation voltages in ternary TMFs (i.e., Mn, Fe, Co, and Ni systems). Additionally, we observed that the linear response theory, when used in conjunction with metaGGA functionals, can give rise to unphysical  $U$  corrections, particularly for TMs with low oxidation states. Overall, our study signifies the importance of adding an optimal  $U$  correction to both SCAN and r<sup>2</sup>SCAN functionals to enhance the accuracy of predicting redox behavior in TMFs. We hope that our study will spur screening studies with higher accuracy in the chemical space of TMFs, which can result in the identification of novel materials for various applications.

All computed data that has been presented in this work are available to the public in our GitHub repository [148].

## ACKNOWLEDGMENTS

G.S.G. acknowledges financial support from the Indian Institute of Science (IISc) Seed Grant, SG/MHRD/20/0020 and SR/MHRD/20/0013, and support from the Science and Engineering Research Board (SERB) of the Government of India, under Sanction Numbers SRG/2021/000201 and IPA/2021/000007. D.B.T. thanks IISc for financial assistance. The authors acknowledge the computational resources provided by the Supercomputer Education and Research Centre

(SERC), IISc. A portion of the calculations in this work used computational resources of the supercomputer Fugaku provided by RIKEN through the HPCI System Research Project (Project ID hp220393). We acknowledge the National Supercomputing Mission (NSM) for providing computing resources of "PARAM Siddhi-AI," under National PARAM Supercomputing Facility (NPSF), C-DAC, Pune, and supported by the Ministry of Electronics and Information Technology (MeitY) and Department of Science and Technology (DST), Government of India.

- [1] R. Dubrovin, L. Alyabyeva, N. Siverin, B. Gorshunov, N. Novikova, K. Boldyrev, and R. Pisarev, Incipient multiferroicity in pnma fluoroperovskite  $\text{NaMnF}_3$ , *Phys. Rev. B* **101**, 180403(R) (2020).
- [2] R. Dubrovin, S. Kizhaev, P. Syrnikov, J.-Y. Gesland, and R. Pisarev, Unveiling hidden structural instabilities and magnetodielectric effect in manganese fluoroperovskites  $\text{AMnF}_3$ , *Phys. Rev. B* **98**, 060403(R) (2018).
- [3] J. Zheng, X. Wang, X. Xiao, H. Cheng, L. Zhang, and L. Chen, Improved reversible dehydrogenation properties of  $\text{Mg}(\text{BH}_4)_2$  catalyzed by dual-cation transition metal fluorides  $\text{K}_2\text{TiF}_6$  and  $\text{K}_2\text{NbF}_7$ , *Chem. Eng. J.* **412**, 128738 (2021).
- [4] M. Wang, Z. Wang, M. Shan, J. Wang, Z. Qiu, J. Song, and Z. Li, Fluorine-substituted donor-acceptor covalent organic frameworks for efficient photocatalyst hydrogen evolution, *Chem. Mater.* **35**, 5368 (2023).
- [5] D. Ali, S. T. Amjad, Z. Shafique, M. M. Naseer, M. Al-Rashida, T. A. Sindhu, S. Iftikhar, M. R. Shah, A. Hameed, and J. Iqbal, Utilization of transition metal fluoride-based solid support catalysts for the synthesis of sulfonamides: Carbonic anhydrase inhibitory activity and in silico study, *RSC Adv.* **12**, 3165 (2022).
- [6] H. Han, J. Woo, Y.-R. Hong, Y.-C. Chung, and S. Mhin, Polarized electronic configuration in transition metal-fluoride oxide hollow nanoprism for highly efficient and robust water splitting, *ACS Appl. Energy Mater.* **2**, 3999 (2019).
- [7] A. C. Garcia-Castro, A. H. Romero, and E. Bousquet, Strain-engineered multiferroicity in *Pnma*  $\text{NaMnF}_3$  fluoroperovskite, *Phys. Rev. Lett.* **116**, 117202 (2016).
- [8] P. Borisov, T. A. Johnson, A. C. García-Castro, A. KC, D. Schrecongost, C. Cen, A. H. Romero, and D. Lederman, Multiferroic  $\text{BaCoF}_4$  in thin film form: Ferroelectricity, magnetic ordering, and strain, *ACS Appl. Mater. Interfaces* **8**, 2694 (2016).
- [9] S. A. Reisinger, M. Leblanc, A.-M. Mercier, C. C. Tang, J. E. Parker, F. D. Morrison, and P. Lightfoot, Phase separation and phase transitions in multiferroic  $\text{K}_{0.5}\text{8FeF}_3$  with the tetragonal tungsten bronze structure, *Chem. Mater.* **23**, 5440 (2011).
- [10] F. Wang, S.-W. Kim, D.-H. Seo, K. Kang, L. Wang, D. Su, J. J. Vajo, J. Wang, and J. Graetz, Ternary metal fluorides as high-energy cathodes with low cycling hysteresis, *Nat. Commun.* **6**, 6668 (2015).
- [11] N. Zhang, X. Xiao, and H. Pang, Transition metal (Fe, Co, Ni) fluoride-based materials for electrochemical energy storage, *Nanoscale Horiz.* **4**, 99 (2019).
- [12] H. Park, Y. Lee, M.-k. Cho, J. Kang, W. Ko, Y. H. Jung, T.-Y. Jeon, J. Hong, H. Kim, and S.-T. Myung,  $\text{Na}_2\text{Fe}_2\text{F}_7$ : A fluoride-based cathode for high power and long life Na-ion batteries, *Energy Environ. Sci.* **14**, 1469 (2021).
- [13] E. E. Foley, V. C. Wu, W. Jin, W. Cui, E. Yoshida, A. Manche, and R. J. Clément, Polymorphism in weberite  $\text{Na}_2\text{Fe}_2\text{F}_7$  and its effects on electrochemical properties as a Na-ion cathode, *Chem. Mater.* **35**, 3614 (2023).
- [14] T. Lu, S. Meng, and M. Liu, Weberite  $\text{Na}_2\text{MM}'\text{F}_7$  (M, M' = redox-active metal) as promising fluoride-based sodium-ion battery cathodes, *J. Mater. Chem. A* **12**, 14709 (2024).
- [15] U. K. Dey, N. Barman, S. Ghosh, S. Sarkar, S. C. Peter, and P. Senguttuvan, Topochemical bottom-up synthesis of 2D- and 3D-sodium iron fluoride frameworks, *Chem. Mater.* **31**, 295 (2019).
- [16] I. Hwang, S.-K. Jung, E.-S. Jeong, H. Kim, S.-P. Cho, K. Ku, H. Kim, W.-S. Yoon, and K. Kang,  $\text{NaF-FeF}_2$  nanocomposite: New type of Na-ion battery cathode material, *Nano Res.* **10**, 4388 (2017).
- [17] S.-W. Kim, D.-H. Seo, H. Gwon, J. Kim, and K. Kang, Fabrication of  $\text{FeF}_3$  nanoflowers on CNT branches and their application to high power lithium rechargeable batteries, *Adv. Mater.* **22**, 5260 (2010).
- [18] X. Hua, A. S. Eggeman, E. Castillo-Martínez, R. Robert, H. S. Geddes, Z. Lu, C. J. Pickard, W. Meng, K. M. Wiaderek, and N. Pereira, Revisiting metal fluorides as lithium-ion battery cathodes, *Nat. Mater.* **20**, 841 (2021).
- [19] A. Manthiram and J. Goodenough, Lithium insertion into  $\text{Fe}_2(\text{SO}_4)_3$  frameworks, *J. Power Sources* **26**, 403 (1989).
- [20] X. Fan, E. Hu, X. Ji, Y. Zhu, F. Han, S. Hwang, J. Liu, S. Bak, Z. Ma, and T. Gao, High energy-density and reversibility of iron fluoride cathode enabled via an intercalation-extrusion reaction, *Nat. Commun.* **9**, 2324 (2018).
- [21] A. Martin, M.-L. Doublet, E. Kemnitz, and N. Pinna, Reversible sodium and lithium insertion in iron fluoride perovskites, *Adv. Funct. Mater.* **28**, 1802057 (2018).
- [22] D. Cao, C. Yin, D. Shi, Z. Fu, J. Zhang, and C. Li, Cubic perovskite fluoride as open framework cathode for Na-ion batteries, *Adv. Funct. Mater.* **27**, 1701130 (2017).
- [23] A. Kitajou, Y. Ishado, T. Yamashita, H. Momida, T. Oguchi, and S. Okada, Cathode properties of perovskite-type  $\text{NaMF}_3$  (M = Fe, Mn, and Co) prepared by mechanical ball milling for sodium-ion battery, *Electrochim. Acta* **245**, 424 (2017).
- [24] Y.-W. Byeon, M.-J. Gong, Z. Cai, Y. Sun, N. J. Szymanski, J. Bai, D.-H. Seo, and H. Kim, Effects of cation and anion

- substitution in  $\text{KVPO}_4\text{F}$  for K-ion batteries, *Energy Storage Materials* **57**, 81 (2023).
- [25] T. Li, L. Li, Y. L. Cao, X. P. Ai, and H. X. Yang, Reversible three-electron redox behaviors of  $\text{FeF}_3$  nanocrystals as high-capacity cathode-active materials for Li-ion batteries, *J. Phys. Chem. C* **114**, 3190 (2010).
- [26] J. Kim, H. Kim, and K. Kang, Conversion-based cathode materials for rechargeable sodium batteries, *Adv. Energy Mater.* **8**, 1702646 (2018).
- [27] X. Fan, Y. Zhu, C. Luo, T. Gao, L. Suo, S.-C. Liou, K. Xu, and C. Wang, In situ lithiated  $\text{FeF}_3/\text{C}$  nanocomposite as high energy conversion-reaction cathode for lithium-ion batteries, *J. Power Sources* **307**, 435 (2016).
- [28] S.-K. Jung, I. Hwang, S.-P. Cho, K. Oh, K. Ku, I. R. Choi, and K. Kang, New iron-based intercalation host for lithium-ion batteries, *Chem. Mater.* **30**, 1956 (2018).
- [29] D. B. Tekliye, A. Kumar, X. Weihang, T. D. Mercy, P. Canepa, and G. Sai Gautam, Exploration of NaSICON frameworks as calcium-Ion battery electrodes, *Chem. Mater.* **34**, 10133 (2022).
- [30] W. Lu, J. Wang, G. Sai Gautam, and P. Canepa, Searching ternary oxides and chalcogenides as positive electrodes for calcium batteries, *Chem. Mater.* **33**, 5809 (2021).
- [31] L. Cheng, R. S. Assary, X. Qu, A. Jain, S. P. Ong, N. N. Rajput, K. Persson, and L. A. Curtiss, Accelerating electrolyte discovery for energy storage with high-throughput screening, *J. Phys. Chem. Lett.* **6**, 283 (2015).
- [32] G. Sai Gautam, E. B. Stechel, and E. A. Carter, Exploring Ca–Ce–M–O ( $M = 3d$  transition metal) oxide perovskites for solar thermochemical applications, *Chem. Mater.* **32**, 9964 (2020).
- [33] W. Sun, C. J. Bartel, E. Arca, S. R. Bauers, B. Matthews, B. Orvañanos, B.-R. Chen, M. F. Toney, L. T. Schelhas, and W. Tumas, A map of the inorganic ternary metal nitrides, *Nat. Mater.* **18**, 732 (2019).
- [34] S. Chakraborty, W. Xie, N. Mathews, M. Sherburne, R. Ahuja, M. Asta, and S. G. Mhaisalkar, Rational design: A high-throughput computational screening and experimental validation methodology for lead-free and emergent hybrid perovskites, *ACS Energy Lett.* **2**, 837 (2017).
- [35] P. Hohenberg and W. Kohn, Inhomogeneous electron gas, *Phys. Rev.* **136**, B864 (1964).
- [36] W. Kohn and L. J. Sham, Self-consistent equations including exchange and correlation effects, *Phys. Rev.* **140**, A1133 (1965).
- [37] J. P. Perdew, K. Burke, and M. Ernzerhof, Generalized gradient approximation made simple, *Phys. Rev. Lett.* **77**, 3865 (1996).
- [38] J. Sun, A. Ruzsinszky, and J. P. Perdew, Strongly constrained and appropriately normed semilocal density functional, *Phys. Rev. Lett.* **115**, 036402 (2015).
- [39] A. P. Bartók and J. R. Yates, Regularized SCAN functional, *J. Chem. Phys.* **150**, 161101 (2019).
- [40] J. W. Furness, A. D. Kaplan, J. Ning, J. P. Perdew, and J. Sun, Accurate and numerically efficient  $r^2\text{SCAN}$  meta-generalized gradient approximation, *J. Phys. Chem. Lett.* **11**, 8208 (2020).
- [41] R. Car, Fixing Jacob's ladder, *Nat. Chem.* **8**, 820 (2016).
- [42] J. H. Yang, D. A. Kitchaev, and G. Ceder, Rationalizing accurate structure prediction in the meta-GGA SCAN functional, *Phys. Rev. B* **100**, 035132 (2019).
- [43] Y. Yao and Y. Kanai, Plane-wave pseudopotential implementation and performance of SCAN meta-GGA exchange-correlation functional for extended systems, *J. Chem. Phys.* **146**, 224105 (2017).
- [44] H.-D. Saßnick and C. Cocchi, Electronic structure of cesium-based photocathode materials from density functional theory: Performance of PBE, SCAN, and HSE06 functionals, *Electron. Struct.* **3**, 027001 (2021).
- [45] Y. Fu and D. J. Singh, Density functional methods for the magnetism of transition metals: SCAN in relation to other functionals, *Phys. Rev. B* **100**, 045126 (2019).
- [46] R. Kingsbury, A. S. Gupta, C. J. Bartel, J. M. Munro, S. Dwaraknath, M. Horton, and K. A. Persson, Performance comparison of  $r^2\text{SCAN}$  and SCAN metaGGA density functionals for solid materials via an automated, high-throughput computational workflow, *Phys. Rev. Mater.* **6**, 013801 (2022).
- [47] S. Swathilakshmi, R. Devi, and G. Sai Gautam, Performance of the  $r^2\text{SCAN}$  functional in transition metal oxides, *J. Chem. Theory Comput.* **19**, 4202 (2023).
- [48] M. J. DelloStretto, A. D. Kaplan, J. P. Perdew, and M. L. Klein, Predicting the properties of nio with density functional theory: Impact of exchange and correlation approximations and validation of the  $r^2\text{SCAN}$  functional, *APL Mater.* **11**, 060702 (2023).
- [49] W. Sun, A. Holder, B. Orvañanos, E. Arca, A. Zakutayev, S. Lany, and G. Ceder, Thermodynamic routes to novel metastable nitrogen-rich nitrides, *Chem. Mater.* **29**, 6936 (2017).
- [50] Z. Deng, T. P. Mishra, E. Mahayoni, Q. Ma, A. J. K. Tieu, O. Guillon, J.-N. Chotard, V. Seznec, A. K. Cheetham, and C. Masquelier, Fundamental investigations on the sodium-ion transport properties of mixed polyanion solid-state battery electrolytes, *Nat. Commun.* **13**, 4470 (2022).
- [51] J. Ning, J. W. Furness, and J. Sun, Reliable lattice dynamics from an efficient density functional approximation, *Chem. Mater.* **34**, 2562 (2022).
- [52] M. Kothakonda, Y. Zhu, Y. Guan, J. He, J. Kidd, R. Zhang, J. Ning, V. Gopalan, W. Xie, and Z. Mao, High-throughput screening assisted discovery of a stable layered anti-ferromagnetic semiconductor:  $\text{CdFeP}_2\text{Se}_6$ , *Adv. Funct. Mater.* **33**, 2210965 (2023).
- [53] R. Devi, B. Singh, P. Canepa, and G. Sai Gautam, Effect of exchange-correlation functionals on the estimation of migration barriers in battery materials, *npj Comput. Mater.* **8**, 160 (2022).
- [54] P. K. Jha, S. N. Totade, P. Barpanda, and G. Sai Gautam, Evaluation of P3-type layered oxides as K-ion battery cathodes, *Inorg. Chem.* **62**, 14971 (2023).
- [55] J. Kumar and G. S. Gautam, Study of pnictides for photovoltaic applications, *Phys. Chem. Chem. Phys.* **25**, 9626 (2023).
- [56] J. P. Perdew and A. Zunger, Self-interaction correction to density-functional approximations for many-electron systems, *Phys. Rev. B* **23**, 5048 (1981).
- [57] G. Sai Gautam and E. A. Carter, Evaluating transition metal oxides within DFT-SCAN and SCAN+U frameworks for solar thermochemical applications, *Phys. Rev. Mater.* **2**, 095401 (2018).

- [58] O. Y. Long, G. Sai Gautam, and E. A. Carter, Evaluating optimal  $U$  for 3d transition-metal oxides within the SCAN+ $U$  framework, *Phys. Rev. Mater.* **4**, 045401 (2020).
- [59] O. Y. Long, G. S. Gautam, and E. A. Carter, Assessing cathode property prediction via exchange-correlation functionals with and without long-range dispersion corrections, *Phys. Chem. Chem. Phys.* **23**, 24726 (2021).
- [60] V. I. Anisimov, J. Zaanen, and O. K. Andersen, Band theory and Mott insulators: Hubbard  $U$  instead of Stoner  $I$ , *Phys. Rev. B* **44**, 943 (1991).
- [61] I. Timrov, N. Marzari, and M. Cococcioni, Hubbard parameters from density-functional perturbation theory, *Phys. Rev. B* **98**, 085127 (2018).
- [62] F. Zhou, M. Cococcioni, C. A. Marianetti, D. Morgan, and G. Ceder, First-principles prediction of redox potentials in transition-metal compounds with LDA+ $U$ , *Phys. Rev. B* **70**, 235121 (2004).
- [63] G. C. Moore, M. K. Horton, E. Linscott, A. M. Ganose, M. Siron, D. D. O'Regan, and K. A. Persson, High-throughput determination of hubbard  $U$  and Hund  $J$  values for transition metal oxides via the linear response formalism, *Phys. Rev. Mater.* **8**, 014409 (2024).
- [64] G. Lan, J. Song, and Z. Yang, A linear response approach to determine Hubbard  $U$  and its application to evaluate properties of  $Y_2B_2O_7$ ,  $B =$  transition metals 3d, 4d and 5d, *J. Alloys Compd.* **749**, 909 (2018).
- [65] M. Shishkin and H. Sato, Self-consistent parametrization of DFT+ $U$  framework using linear response approach: Application to evaluation of redox potentials of battery cathodes, *Phys. Rev. B* **93**, 085135 (2016).
- [66] N. J. Mosey and E. A. Carter, *Ab initio* evaluation of Coulomb and exchange parameters for DFT+ $U$  calculations, *Phys. Rev. B* **76**, 155123 (2007).
- [67] N. J. Mosey, P. Liao, and E. A. Carter, Rotationally invariant *ab initio* evaluation of coulomb and exchange parameters for DFT+ $U$  calculations, *J. Chem. Phys.* **129**, 014103 (2008).
- [68] F. Aryasetiawan and O. Gunnarsson, Electronic structure of NiO in the GW approximation, *Phys. Rev. Lett.* **74**, 3221 (1995).
- [69] L. A. Agapito, S. Curtarolo, and M. Buongiorno Nardelli, Reformulation of DFT+ $U$  as a pseudohybrid Hubbard density functional for accelerated materials discovery, *Phys. Rev. X* **5**, 011006 (2015).
- [70] M. Yu, S. Yang, C. Wu, and N. Marom, Machine learning the Hubbard  $U$  parameter in DFT+ $U$  using Bayesian optimization, *npj Comput. Mater.* **6**, 180 (2020).
- [71] N. Artrith, J. A. Garrido Torres, A. Urban, and M. S. Hybertsen, Data-driven approach to parameterize SCAN +  $U$  for an accurate description of 3d transition metal oxide thermochemistry, *Phys. Rev. Mater.* **6**, 035003 (2022).
- [72] L. Wang, T. Maxisch, and G. Ceder, Oxidation energies of transition metal oxides within the GGA+ $U$  framework, *Phys. Rev. B* **73**, 195107 (2006).
- [73] A. Jain, G. Hautier, S. P. Ong, C. J. Moore, C. C. Fischer, K. A. Persson, and G. Ceder, Formation enthalpies by mixing GGA and GGA+ $U$  calculations, *Phys. Rev. B* **84**, 045115 (2011).
- [74] S. Lutfalla, V. Shapovalov, and A. T. Bell, Calibration of the DFT/GGA+ $U$  method for determination of reduction energies for transition and rare earth metal oxides of Ti, V, Mo, and Ce, *J. Chem. Theory Comput.* **7**, 2218 (2011).
- [75] C. Loschen, J. Carrasco, K. M. Neyman, and F. Illas, First-principles LDA+ $U$  and GGA+ $U$  study of cerium oxides: Dependence on the effective  $U$  parameter, *Phys. Rev. B* **75**, 035115 (2007).
- [76] S. Curtarolo, G. L. Hart, M. B. Nardelli, N. Mingo, S. Sanvito, and O. Levy, The high-throughput highway to computational materials design, *Nat. Mater.* **12**, 191 (2013).
- [77] Z. Lun, B. Ouyang, D.-H. Kwon, Y. Ha, E. E. Foley, T.-Y. Huang, Z. Cai, H. Kim, M. Balasubramanian, and Y. Sun, Cation-disordered rocksalt-type high-entropy cathodes for Li-ion batteries, *Nat. Mater.* **20**, 214 (2021).
- [78] C. J. Bartel, A. W. Weimer, S. Lany, C. B. Musgrave, and A. M. Holder, The role of decomposition reactions in assessing first-principles predictions of solid stability, *npj Comput. Mater.* **5**, 4 (2019).
- [79] P. Zhong, F. Xie, L. Barroso-Luque, L. Huang, and G. Ceder, Modeling intercalation chemistry with multiredox reactions by sparse lattice models in disordered rocksalt cathodes, *PRX Energy* **2**, 043005 (2023).
- [80] G. Kresse and J. Hafner, *Ab initio* molecular dynamics for liquid metals, *Phys. Rev. B* **47**, 558 (1993).
- [81] G. Kresse and J. Furthmüller, Efficient iterative schemes for *ab initio* total-energy calculations using a plane-wave basis set, *Phys. Rev. B* **54**, 11169 (1996).
- [82] G. Kresse and D. Joubert, From ultrasoft pseudopotentials to the projector augmented-wave method, *Phys. Rev. B* **59**, 1758 (1999).
- [83] P. E. Blöchl, Projector augmented-wave method, *Phys. Rev. B* **50**, 17953 (1994).
- [84] See Supplemental Material at <http://link.aps.org/supplemental/10.1103/PhysRevMaterials.8.093801> for oxidation energetics of Cr, Mn, Ni and Cu fluorides, magnetic configurations of TMFs, projector augmented wave potentials used, optimized  $U$  with experimental data at 298 K and 0 K, lattice parameters, on-site magnetic moments and band gaps, calculated electronic densities of states and band gap comparisons, powder colors and associated band gaps of TMFs, average voltage calculations, linear response theory and hybrid functional calculations, charge density differences, convex hulls, and comparison of calculated and experimental properties for V- and Fe-fluorides with  $U$  optimized using 298 K and 0 K experimental data.
- [85] S. L. Dudarev, G. A. Botton, S. Y. Savrasov, C. Humphreys, and A. P. Sutton, Electron-energy-loss spectra and the structural stability of nickel oxide: An LSDA+ $U$  study, *Phys. Rev. B* **57**, 1505 (1998).
- [86] H. J. Monkhorst and J. D. Pack, Special points for Brillouin-zone integrations, *Phys. Rev. B* **13**, 5188 (1976).
- [87] M. Hellenbrandt, The inorganic crystal structure database (ICSD)—Present and future, *Crystallog. Rev.* **10**, 17 (2004).
- [88] E. Wollan, H. Child, W. Koehler, and M. Wilkinson, Antiferromagnetic properties of the iron group trifluorides, *Phys. Rev.* **112**, 1132 (1958).
- [89] J. P. Perdew, W. Yang, K. Burke, Z. Yang, E. K. Gross, M. Scheffler, G. E. Scuseria, T. M. Henderson, I. Y. Zhang, and A. Ruzsinszky, Understanding band gaps of solids in generalized Kohn–Sham theory, *Proc. Natl. Acad. Sci. USA* **114**, 2801 (2017).



- [90] J. Heyd, G. E. Scuseria, and M. Ernzerhof, Hybrid functionals based on a screened Coulomb potential, *J. Chem. Phys.* **118**, 8207 (2003).
- [91] A. V. Krukau, O. A. Vydrov, A. F. Izmaylov, and G. E. Scuseria, Influence of the exchange screening parameter on the performance of screened hybrid functionals, *J. Chem. Phys.* **125**, 224106 (2006).
- [92] M. W. Chase, Jr., C. A. Davies, J. R. Downey, Jr., D. J. Frurip, R. A. McDonald, and A. N. Syverud, *NIST-JANAF Thermochemical Tables*, American Chemical Society (National Institute of Standards and Technology, New York, 1998).
- [93] O. Kubaschewski, C. B. Alcock, and P. J. Spencer, *Materials Thermochemistry*, 6th ed. (Pergamon Press Ltd., Oxford, 1993).
- [94] I. Barin, *Thermochemical Data of Pure Substances*, 3rd ed. (John Wiley & Sons, New York, 1995).
- [95] D. D. Wagman, *The NBS Tables of Chemical Thermodynamic Properties: Selected Values for Inorganic and C1 and C2 Organic Substances in SI Units* (American Chemical Society and the American Institute of Physics for the National Bureau of Standards, Washington, DC, 1982).
- [96] G. K. Johnson, The enthalpy of formation of  $\text{FeF}_3$  by fluorine bomb calorimetry, *J. Chem. Thermodyn.* **13**, 465 (1981).
- [97] S. N. Solov'ev, A. Korunov, K. Zubkov, and A. Firer, Standard enthalpy of formation of nickel trifluoride by isothermal calorimetry, *Russ. J. Phys. Chem. A* **86**, 516 (2012).
- [98] M. Aykol and C. Wolverton, Local environment dependent GGA+U method for accurate thermochemistry of transition metal compounds, *Phys. Rev. B* **90**, 115105 (2014).
- [99] M. Cococcioni and S. de Gironcoli, Linear response approach to the calculation of the effective interaction parameters in the LDA+U method, *Phys. Rev. B* **71**, 035105 (2005).
- [100] D. Sheets, K. Lyszak, M. Jain, G. W. Fernando, I. Sochnikov, J. Franklin, J. N. Hancock, and R. M. Geilhufe, Mott insulating low thermal expansion perovskite  $\text{TiF}_3$ , *Phys. Rev. B* **108**, 235140 (2023).
- [101] A. Gossard, F. Di Salvo, W. Falconer, T. Rice, J. Voorhoeve, and H. Yasuoka, Magnetic ordering of a d1 compound:  $\text{VF}_4$ , *Solid State Commun.* **14**, 1207 (1974).
- [102] T. Chatterji and T. C. Hansen, Magnetoelastic effects in Jahn–Teller distorted  $\text{CrF}_2$  and  $\text{CuF}_2$  studied by neutron powder diffraction, *J. Phys.: Condens. Matter* **23**, 276007 (2011).
- [103] J. Stempffer, U. Rütt, S. P. Bayrakci, T. Brückel, and W. Jauch, Magnetic properties of transition metal fluorides  $\text{MF}_2$  ( $M = \text{Mn, Fe, Co, Ni}$ ) via high-energy photon diffraction, *Phys. Rev. B* **69**, 014417 (2004).
- [104] K. Lutar, A. Jesih, and B. Žemva,  $\text{KrF}_2/\text{MnF}_4$  adducts from  $\text{KrF}_2/\text{MnF}_2$  interaction in HF as a route to high purity  $\text{MnF}_4$ , *Polyhedron* **7**, 1217 (1988).
- [105] Z.-h. Yang, X.-y. Wang, L. Li, and X.-p. Su, Structural, magnetic and electronic properties of  $\text{FeF}_2$  by first-principle calculation, *Trans. Nonferrous Met. Soc. China* **22**, 386 (2012).
- [106] T. Chatterji, B. Ouladdiaf, and T. C. Hansen, The magnetoelastic effect in  $\text{CoF}_2$  investigated by means of neutron powder diffraction, *J. Phys.: Condens. Matter* **22**, 096001 (2010).
- [107] S. Lee, S. Torii, Y. Ishikawa, M. Yonemura, T. Moyoshi, and T. Kamiyama, Weak-ferromagnetism of  $\text{CoF}_3$  and  $\text{FeF}_3$ , *Phys. B: Condens. Matter* **551**, 94 (2018).
- [108] T. Chatterji, G. N. Iles, B. Ouladdiaf, and T. C. Hansen, Magnetoelastic effect in  $\text{MF}_2$  ( $M = \text{Mn, Fe, Ni}$ ) investigated by neutron powder diffraction, *J. Phys.: Condens. Matter* **22**, 316001 (2010).
- [109] C. Shen, L. C. Chacón, N. Rosov, S. H. Elder, J. C. Allman, and N. Bartlett, The structure of  $\text{R-NiF}_3$ , and synthesis, and magnetism of new  $\text{R}_3 \text{M}^{\text{II}}\text{Ni}^{\text{IV}}\text{F}_6$  ( $M = \text{Fe, Co, Cu, Zn}$ ), and  $\text{M}^{\text{II}}\text{Ni}^{\text{IV}}\text{F}_4$  ( $M = \text{Co, Cu}$ ), *C. R. Acad. Sci. IIC* **2**, 557 (1999).
- [110] P. Fischer, W. Hälg, D. Schwarzenbach, and H. Gamsjäger, Magnetic and crystal structure of copper (II) fluoride, *J. Phys. Chem. Solids* **35**, 1683 (1974).
- [111] F. Ebert and H. Weitinek, Kristallstrukturen von Fluoriden. II.  $\text{HgF}$ ,  $\text{HgF}_2$ ,  $\text{CuF}$  und  $\text{CuF}_2$ , *Z. Anorg. Allg. Chem.* **210**, 269 (1933).
- [112] W. H. Baur and A. A. Khan, Rutile-type compounds. IV.  $\text{SiO}_2$ ,  $\text{GeO}_2$  and a comparison with other rutile-type structures, *Acta Crystallogr. B* **27**, 2133 (1971).
- [113] W. H. Baur, Über die Verfeinerung der Kristallstrukturbestimmung einiger Vertreter des Rutiltyps. II. Die Difluoride von Mn, Fe, Co, Ni und Zn, *Acta Crystallogr.* **11**, 488 (1958).
- [114] F. M. Brewer, The place of chemistry-I. at Oxford, *Proc. Chem. Soc.*, 185 (1957).
- [115] P. C. Burns and F. C. Hawthorne, Rietveld refinement of the crystal structure of  $\text{CuF}_2$ , *Powder Diffr.* **6**, 156 (1991).
- [116] S. Siegel, The structure of  $\text{TiF}_3$ , *Acta Crystallogr.* **9**, 684 (1956).
- [117] K. Jack and V. Gutmann, The crystal structure of vanadium trifluoride  $\text{VF}_3$ , *Acta Crystallogr.* **4**, 246 (1951).
- [118] K. Knox, Structures of chromium (III) fluoride, *Acta Crystallogr.* **13**, 507 (1960).
- [119] M. Hepworth, K. Jack, R. Peacock, and G. Westland, The crystal structures of the trifluorides of iron, cobalt, ruthenium, rhodium, palladium and iridium, *Acta Crystallogr.* **10**, 63 (1957).
- [120] M. Leblanc, J. Pannetier, G. Ferey, and R. De Pape, Single crystal refinement of the structure of rhombohedral  $\text{FeF}_3$ , *Rev. Chim. Miner.* **16**, 107 (1985).
- [121] M. A. Hepworth and K. H. Jack, The crystal structure of manganese trifluoride,  $\text{MnF}_3$ , *Acta Crystallogr.* **10**, 345 (1957).
- [122] H. Bialowons, M. Müller, and B. Müller, Titanatetrafluorid—Eine überraschend einfache Kolumnarstruktur, *Z. Anorg. Allg. Chem.* **621**, 1227 (1995).
- [123] S. Becker and B. G. Müller, Vanadiumtetrafluorid, *Angew. Chem.* **102**, 426 (1990).
- [124] O. Krämer and B. Müller, Zur Struktur des Chromtetrafluorids, *Z. Anorg. Allg. Chem.* **621**, 1969 (1995).
- [125] B. G. Müller and M. Serafin, Die Kristallstruktur von Manganatetrafluorid [The crystal/structure of manganese tetrafluoride], *Z. Naturforsch. B* **42**, 1102 (1987).
- [126] V. L. Campo and M. Cococcioni, Extended DFT+U+V method with on-site and inter-site electronic interactions, *J. Phys.: Condens. Matter* **22**, 055602 (2010).
- [127] S.-H. Lee and Y.-W. Son, First-principles approach with a pseudohybrid density functional for extended Hubbard interactions, *Phys. Rev. Res.* **2**, 043410 (2020).
- [128] B. Himmetoglu, R. M. Wentzcovitch, and M. Cococcioni, First-principles study of electronic and structural properties of  $\text{CuO}$ , *Phys. Rev. B* **84**, 115108 (2011).

- [129] H. Hsu, K. Umemoto, M. Cococcioni, and R. Wentzcovitch, First-principles study for low-spin  $\text{LaCoO}_3$  with a structurally consistent Hubbard  $U$ , *Phys. Rev. B* **79**, 125124 (2009).
- [130] D. R. Lide, *CRC Handbook of Chemistry and Physics*, Vol. 85 (CRC Press Boca Raton, FL, 2004).
- [131] F. Kraus, S. I. Ivlev, J. Bandemehr, M. Sachs, C. Pietzonka, M. Conrad, M. Serafin, and B. G. Müller, Synthesis and characterization of manganese tetrafluoride  $\beta - \text{MnF}_4$ , *Z. Anorg. Allg. Chem.* **646**, 1481 (2020).
- [132] M. Nikitin and A. Alikhanyan, Thermochemistry of nickel trifluoride, *Russ. J. Inorg. Chem.* **64**, 641 (2019).
- [133] R. E. Hummel, *Electronic Properties of Materials* (Springer, New York, 2011).
- [134] A. Devey, R. Grau-Crespo, and N. de Leeuw, Electronic and magnetic structure of  $\text{Fe}_3\text{S}_4$ : GGA+ $U$  investigation, *Phys. Rev. B* **79**, 195126 (2009).
- [135] S. Rodríguez, C. Zandalazini, J. Navarro, K. Vadiraj, and E. Albanesi, First principles calculations and experimental study of the optical properties of Ni-doped  $\text{ZnS}$ , *Mater. Res. Express* **7**, 016303 (2020).
- [136] D.-H. Seo, A. Urban, and G. Ceder, Calibrating transition-metal energy levels and oxygen bands in first-principles calculations: Accurate prediction of redox potentials and charge transfer in lithium transition-metal oxides, *Phys. Rev. B* **92**, 115118 (2015).
- [137] S. Mattsson and B. Paulus, Density functional theory calculations of structural, electronic, and magnetic properties of the 3d metal trifluorides  $\text{MF}_3$  ( $M = \text{Ti-Ni}$ ) in the solid state, *J. Comput. Chem.* **40**, 1190 (2019).
- [138] N. Dimov, A. Nishimura, K. Chihara, A. Kitajou, I. D. Gocheva, and S. Okada, Transition metal  $\text{NaMF}_3$  compounds as model systems for studying the feasibility of ternary Li-MF and Na-MF single phases as cathodes for lithium-ion and sodium-ion batteries, *Electrochim. Acta* **110**, 214 (2013).
- [139] W. Sun, S. T. Dacek, S. P. Ong, G. Hautier, A. Jain, W. D. Richards, A. C. Gamst, K. A. Persson, and G. Ceder, The thermodynamic scale of inorganic crystalline metastability, *Sci. Adv.* **2**, e1600225 (2016).
- [140] K.-H. Wandner and R. Hoppe, Zur Kenntnis von  $\text{NaMn}_3\text{F}_{10}$ , *Z. Anorg. Allg. Chem.* **549**, 7 (1987).
- [141] F. L. M. Bernal, B. Gonano, F. Lundvall, D. S. Wragg, H. Fjellvåg, F. Veillon, W. A. Sławiński, and O. S. Fjellvåg, Canted antiferromagnetism in high-purity  $\text{NaFeF}_3$  prepared by a novel wet-chemical synthesis method, *Phys. Rev. Mater.* **4**, 114412 (2020).
- [142] I. Timrov, F. Aquilante, M. Cococcioni, and N. Marzari, Accurate electronic properties and intercalation voltages of olivine-type Li-ion cathode materials from extended Hubbard functionals, *PRX Energy* **1**, 033003 (2022).
- [143] C. Ricca, I. Timrov, M. Cococcioni, N. Marzari, and U. Aschauer, Self-consistent DFT +  $U$  +  $V$  study of oxygen vacancies in  $\text{SrTiO}_3$ , *Phys. Rev. Res.* **2**, 023313 (2020).
- [144] N. Tancogne-Dejean and A. Rubio, Parameter-free hybridlike functional based on an extended Hubbard model: DFT+ $U$ + $V$ , *Phys. Rev. B* **102**, 155117 (2020).
- [145] M. L. Tiago, S. Ismail-Beigi, and S. G. Louie, Effect of semicore orbitals on the electronic band gaps of Si, Ge, and GaAs within the GW approximation, *Phys. Rev. B* **69**, 125212 (2004).
- [146] M. Oshikiri and F. Aryasetiawan, Band gaps and quasiparticle energy calculations on  $\text{ZnO}$ ,  $\text{ZnS}$ , and  $\text{ZnSe}$  in the zinc-blende structure by the GW approximation, *Phys. Rev. B* **60**, 10754 (1999).
- [147] R. S. Kingsbury, A. S. Rosen, A. S. Gupta, J. M. Munro, S. P. Ong, A. Jain, S. Dwaraknath, M. K. Horton, and K. A. Persson, A flexible and scalable scheme for mixing computed formation energies from different levels of theory, *npj Comput. Mater.* **8**, 195 (2022).
- [148] <https://github.com/sai-mat-group/fluorides-benchmarking>.